

# Neutrons from projectile fragmentation at 600 MeV/nucleon

P. Pawłowski,<sup>1</sup> J. Brzychczyk,<sup>2</sup> N. Buyukcizmeci,<sup>3</sup> H. T. Johansson,<sup>4</sup> W. Trautmann,<sup>5</sup> A. Wieloch,<sup>2</sup> P. Adrich,<sup>6</sup> T. Aumann,<sup>5</sup> T. Barczyk,<sup>2,\*</sup> S. Bianchin,<sup>5</sup> K. Boretzky,<sup>5</sup> A. S. Botvina,<sup>7,8</sup> A. Chbihi,<sup>9</sup> J. Cibor,<sup>1</sup> B. Czech,<sup>1</sup> H. Emling,<sup>5</sup> J. D. Frankland,<sup>9</sup> M. Heil,<sup>5</sup> A. Le Fèvre,<sup>5</sup> Y. Leifels,<sup>5</sup> J. Lühning,<sup>5</sup> J. Lukasik,<sup>1,5</sup> U. Lynen,<sup>5</sup> Z. Majka,<sup>2</sup> I. N. Mishustin,<sup>10</sup> W. F. J. Müller,<sup>5</sup> R. Ogul,<sup>3</sup> H. Orth,<sup>5</sup> R. Palit,<sup>5</sup> D. Rossi,<sup>5</sup> C. Schwarz,<sup>5</sup> C. Sienti,<sup>11</sup> H. Simon,<sup>5</sup> K. Sümmerer,<sup>5</sup> H. Weick,<sup>5</sup> and B. Zwiegliński<sup>6</sup>

<sup>1</sup>*H. Niewodniczański Institute of Nuclear Physics, PL-31342 Kraków, Poland*

<sup>2</sup>*M. Smoluchowski Institute of Physics, Jagiellonian University, PL-30059 Kraków, Poland*

<sup>3</sup>*Department of Physics, University of Selçuk, TR-42079 Konya, Turkey*

<sup>4</sup>*Chalmers University of Technology, Kemivägen 9, S-412 96 Göteborg, Sweden*

<sup>5</sup>*GSI Helmholtzzentrum für Schwerionenforschung GmbH, D-64291 Darmstadt, Germany*

<sup>6</sup>*National Centre for Nuclear Research, PL-02093 Warsaw, Poland*

<sup>7</sup>*Institute for Theoretical Physics, J. W. Goethe University, D-60438 Frankfurt am Main, Germany*

<sup>8</sup>*Helmholtz Research Academy Hesse for FAIR (HFHF), Max-von-Laue-Str. 12, D-60438 Frankfurt am Main, Germany*

<sup>9</sup>*GANIL, CEA et IN2P3-CNRS, F-14076 Caen, France*

<sup>10</sup>*Frankfurt Institute for Advanced Studies, J.W. Goethe University, D-60438 Frankfurt am Main, Germany*

<sup>11</sup>*Institute of Nuclear Physics, Johannes Gutenberg University, D-55099 Mainz, Germany*

(Dated: October 3, 2023)

The neutron emission in projectile fragmentation at relativistic energies was studied with the Large-Area-Neutron-Detector LAND coupled to the ALADIN forward spectrometer at the GSI Schwerionen-Synchrotron (SIS). Stable  $^{124}\text{Sn}$  and radioactive  $^{107}\text{Sn}$  and  $^{124}\text{La}$  beams with an incident energy of 600 MeV/nucleon were used to explore the  $N/Z$  dependence of the identified neutron source. A cluster-recognition algorithm is applied for identifying individual particles within the hit distributions registered with LAND. The obtained momentum distributions are extrapolated over the full phase space occupied by the neutrons from the projectile-spectator source. The mean multiplicities of spectator neutrons reach values of up to about 11 and depend strongly on the isotopic composition of the projectile. An effective source temperature of  $T \approx 2 - 5$  MeV, monotonically increasing with decreasing impact parameter, is deduced from the transverse momentum distributions. For the interpretation of the data, calculations with the statistical multifragmentation model were performed. The variety of excited projectile spectators assumed to decay statistically is represented by an ensemble of excited sources with parameters determined previously from the fragment production observed in the same experiments. The obtained agreement is very satisfactory for more peripheral collisions where, according to the model, neutrons are mainly emitted during the secondary decays of excited fragments. The neutron multiplicity in more central collisions is underestimated, indicating that other sources besides the modeled statistical breakup contribute to the observed neutron yield. The choice made for the symmetry-term coefficient of the liquid-drop description of produced fragments has a weak effect on the predicted neutron multiplicities.

PACS numbers: 25.70.Mn, 25.70.Pq, 24.10.Pa

## I. INTRODUCTION

A comprehensive study of the isospin dependence of projectile fragmentation at relativistic energies has been performed at the GSI Schwerionen-Synchrotron (SIS) with stable and radioactive Sn and La beams of 600 MeV/nucleon [1, 2]. As a primary result, it was found that the fragmentation process as manifested by the recorded fragment distributions and correlations responds only weakly to changes in the projectile composition explored within the interval of neutron-to-proton ratios  $N/Z = 1.16 - 1.48$ . Among global observables, only the isotopic fragment distributions, measured with individual mass resolution up to atomic number  $Z \leq 10$ ,

varied as a function of the projectile  $N/Z$ . Chemical breakup temperatures, as determined from double yield ratios of  $Z = 2 - 4$  isotopes, were in the range of  $T = 4 - 8$  MeV, increasing with decreasing impact parameter, and found to not depend on the isotopic composition of the projectile [1]. Temperatures of  $T \approx 6$  MeV characterize the class of reactions associated with a maximum production of intermediate-mass fragments.

One of the main observations concerned the abundance of neutron-rich fragments in the reaction channels leading to the multifragmentation of the excited projectile-spectator systems. In particular, in the range of fragments with atomic numbers  $6 \leq Z \leq 10$ , the neutron richness of the measured mass distributions exceeded the predictions of the statistical multifragmentation model (SMM, Ref. [3]) whose input parameters had been adjusted to reproduce the measured fragment  $Z$  distributions and correlations. For also correctly reproduc-

\*deceased

ing the mass distributions, a significant reduction of the symmetry-term coefficient in the liquid-drop description of the produced fragments was found to be necessary. This was supported by the isoscaling analysis performed with the same data [2] which confirmed earlier findings for similar reactions [4, 5].

Apart from the fast nucleons emitted during the primary cascade-type stage of the reaction, neutron emission is expected to occur primarily in the form of secondary decays of the excited residue nuclei and fragments. The observed neutron richness of the fragments implies that fewer neutrons are evaporated than one would expect with standard SMM assumptions. The properties of the neutron emission should thus complement the observations made in the fragment channels.

In this paper, we report the results for the projectile-spectator source of neutrons obtained in the same experiments. This was made possible by positioning the Large-Area Neutron Detector LAND [6] downstream of the ALADIN forward spectrometer. The acceptance of LAND covered approximately half of the phase space occupied by neutrons from the projectile decay which was sufficient for identifying the strength and main dynamical properties of the projectile neutron source. For the theoretical interpretation of the experimental findings, SMM calculations [7] were performed. The same ensembles and parameters were used that have previously been determined in the study of fragment production in these reactions [2].

LAND had already been coupled to the ALADIN spectrometer in earlier experiments. The properties of neutron emission obtained in this way have been essential for determining the average energy transfer to the projectile spectator as a function of the impact parameter [8, 9]. The separation energies of neutrons and their kinetic energies in the source frame amount together to a substantial fraction of the total excitation energies of the produced spectator sources (see, e.g., Fig. 7 in Ref. [10]).

Multifragmentation experiments including the measurement of neutrons, even though difficult because of the different techniques required for simultaneously detecting neutral and charged particles, have been performed at several laboratories (see, e.g., Refs. [11–16] and references given therein). Neutron emission in heavy-ion reactions at relativistic energies has been studied with plastic scintillator arrays at the Bevalac by the group of Madey *et al.* in inclusive [17–19] and impact-parameter selected measurements [20, 21]. Together with the present results, they reveal common properties of the neutron emission in spectator fragmentation, as will be shown in the discussion sections.

Results of the ALADIN-LAND experimental study have been used in a variety of different analyses. Besides the statistical description obtained with the SMM and reported in Ref. [2], a dynamical description of the observed fragment production was achieved by Su *et al.* [22]. It is based on calculations using the isospin dependent quantum molecular dynamics (IQMD) model and a min-

imum spanning tree algorithm for recognizing fragments after their formation. The statistical code GEMINI was used to investigate the influence of secondary decays on fragmentation observables.

Very recently, fluctuations up to fourth order of the  $Z$  distributions of the largest fragment in these reactions were investigated with the experimental data as well as statistical calculations with the SMM and the canonical thermodynamic fragmentation model [23]. They were found to exhibit signatures characteristic of a second-order phase transition, established with cubic bond percolation and previously observed for the fragmentation of  $^{197}\text{Au}$  projectiles at similar energies [24]. These signatures depend only weakly on the  $A/Z$  ratio of the fragmenting spectator source. The transition point is characterized by the asymmetry parameter skewness passing through zero and the kurtosis excess simultaneously reaching a minimum. According to the IQMD calculations for these reactions, it is located at fairly peripheral impact parameters  $b = 8.5 - 9.0$  fm [25, 26].

The minor influence of the isotopic composition on general properties of the fragmentation process has emerged as a common observation in all studies made so far [1, 2, 22, 23]. The only exception is the mean neutron-over-proton ratio of intermediate mass fragments found to depend on the neutron richness of the initial projectiles in the present and similar reactions [2, 27–29]. Also for that reason, the properties of the neutron source are of interest and can be expected to provide complementary information.

## II. EXPERIMENTAL DETAILS

### A. ALADIN experiment S254

The ALADIN experiment S254, conducted in 2003 at the SIS heavy-ion synchrotron, has been described in detail in the previous Refs. [1, 2]. Stable  $^{124}\text{Sn}$  and neutron-poor secondary  $^{107}\text{Sn}$  and  $^{124}\text{La}$  beams were used for the study of isotopic and isobaric effects over a wide range of isotopic compositions. The radioactive secondary beams were produced at the fragment separator FRS [30] by fragmenting primary  $^{142}\text{Nd}$  projectiles in a thick beryllium target. To reach the necessary intensities, contributions of neighboring nuclides in addition to the requested isotopes had to be accepted. The mean compositions of the nominal  $^{124}\text{La}$  ( $^{107}\text{Sn}$ ) beams were  $\langle Z \rangle = 56.8$  (49.7) and mass-over-charge ratio  $\langle A/Z \rangle = 2.19$  (2.16), respectively [31]. All beams had a laboratory energy of 600 MeV/nucleon, intensities of about  $10^3$  particles/s, and were directed onto reaction targets consisting of  $^{\text{nat}}\text{Sn}$  with areal density 500 or 1000 mg/cm<sup>2</sup>, corresponding to estimated interaction probabilities slightly exceeding 1% and 2%, respectively.

The ALADIN experimental setup has been described previously [32]. Its configuration in the present experiment is shown in Fig. 1 in the form of a cross-sectional

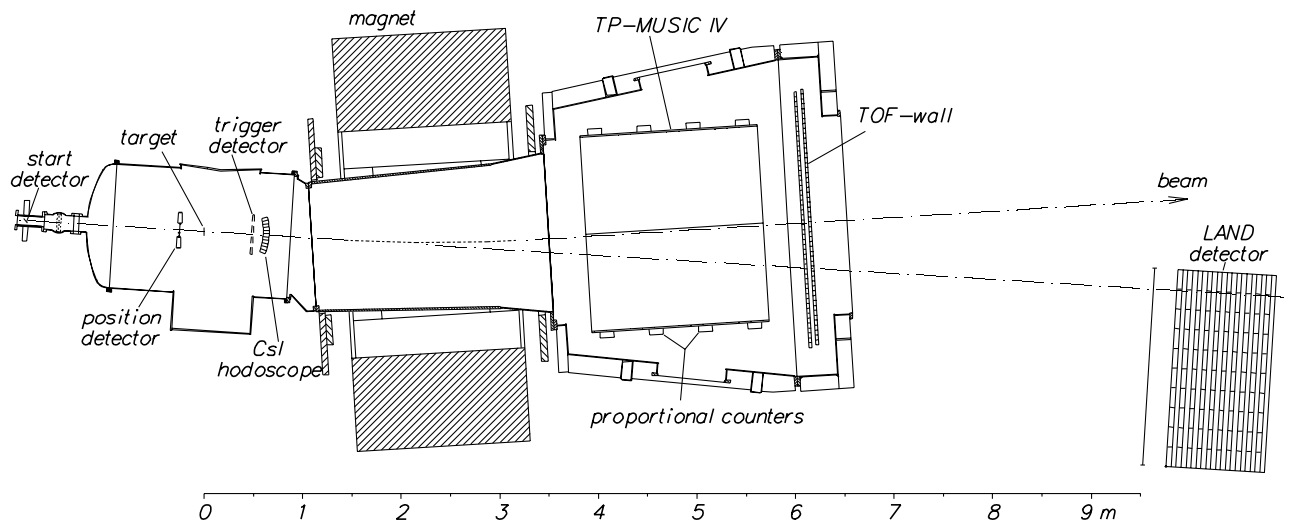


FIG. 1: Setup of the S254 experiment consisting of the ALADIN forward spectrometer and the neutron detector LAND in a cross-sectional view from above onto the plane containing the beam axis. The beam enters from the left. The white rectangles in the magnet indicate the location of the coils. The instrumentation installed in the target chamber is described in Ref. [2]; data from the 84-element CsI hodoscope [33] were not used for the present analysis (reprinted from Ref. [34], Copyright © 2005, with permission from Elsevier).

view from above onto the horizontal plane containing the beam axis. It included three chambers: the target chamber followed by the chamber inserted in between the poles and coils of the window-frame type magnet and the detector chamber. Vacuum is maintained in the target and magnet chambers up to the pressure window separating the volumes of the magnet and detector chambers. The gas pressure in the detector chamber was kept at approximately 1 bar.

Fragment detection and identification was achieved by measuring the atomic number  $Z$ , the magnetic rigidity, and the velocity of the produced fragments with the TP-MUSIC IV detector, upgraded by adding proportional counters to the readout system [35–37], and the ALADIN time-of-flight wall [38]. The threshold for fragment detection and identification was below  $Z = 2$ . The obtained resolution in atomic number was  $\Delta Z \leq 0.6$  (FWHM), independent of  $Z$  up to the projectile  $Z$ . Fragment masses were identified with a resolution of about 3% for fragments with  $Z \leq 3$  (standard deviation), improving to 1.5% for  $Z \geq 6$ , and found to be the same in the experiments with stable and radioactive beams. Masses are thus individually resolved for fragments with  $Z \leq 10$ .

The acceptance of the ALADIN forward spectrometer, in the geometry of the present experiment, was  $\pm 10.2^\circ$  for  $N = Z$  fragments with beam velocity in the horizontal direction, i.e., in the bending plane, and  $\pm 4.5^\circ$  in the vertical direction. The magnetic fields were set to deflect the primary ion beams by an angle of  $7.1^\circ$ . The neutron detector LAND was positioned approximately 10 m downstream from the target, in the vertical direction symmetrically with respect to the incoming beam direction but displaced horizontally away from the direction of the deflected beam (Fig. 1). The intersection point

of the original direction of the incoming beam with the front face of the veto wall of LAND had a distance of 9.65 m from the target and of 22 cm from the left edge of the leftmost paddle of the wall. At this distance, the acceptance of LAND for neutrons emitted from the target position is unobstructed by the pole gap of the ALADIN magnet, except for small regions near the upper, lower, and right edges of the detector. Roughly one half of the phase space occupied by the spectator source of neutrons is covered with LAND in this configuration.

Trigger signals for reactions in the target were derived from four plastic-scintillator paddles positioned approximately 50 cm downstream from the target at angles outside the acceptance of the spectrometer. The condition that at least one of them fired was met with nearly 100% probability by events with moderate to large charged-particle multiplicities [2].

The quantity  $Z_{\text{bound}}$  defined as the sum of the atomic numbers  $Z_i$  of all detected fragments with  $Z_i \geq 2$  was chosen as the principal variable for event sorting. Because of the selective coverage of the projectile-spectator decay,  $Z_{\text{bound}}$  represents approximately the charge of the primary spectator system, apart from emitted hydrogen isotopes, and is monotonically correlated with the impact parameter of the reaction [26, 32, 38]. The excitation energy per nucleon of the spectator system is inversely correlated with  $Z_{\text{bound}}$  [32, 39].

The measurement of neutrons with LAND coupled to the ALADIN spectrometer is characterized by two specific features. One is the use of LAND for reactions producing large neutron multiplicities, which has the effect that the identification of individual neutrons from the hit pattern recorded with the detector is not straightforward. This topic was investigated prior to the final

data analysis, and the obtained results are published in Ref. [40]. The second distinctive item concerns the detection of neutrons originating from the target before the ALADIN spectrometer with considerable amounts of material, mostly iron, being placed in the area between the target and the neutron detector (Fig. 1). The feasibility of a reliable measurement under these conditions was explored with a model study using the Geant4 framework [41] which is reported in detail in the Appendix of this paper. The essential results of both studies and their consequences for the data analysis and achievable accuracy of the measurement are summarized in the following subsections.

### B. LAND detector

The Large-Area-Neutron-Detector LAND is a  $2 \times 2 \times 1$  m<sup>3</sup> calorimeter consisting of in total 200 slabs of interleaved iron and plastic strips viewed by photomultiplier tubes at both ends [6]. A  $2 \times 2$  m<sup>2</sup> veto wall in front of the detector permitted the identification of light charged particles, mainly hydrogen isotopes, hitting the LAND detector. The wall consists of a plane of 20 vertical paddles made of 5-mm-thick plastic scintillators, each 2 m long and 10 cm wide. Their area and orientation are the same as those of the first plane of LAND (Fig. 2).

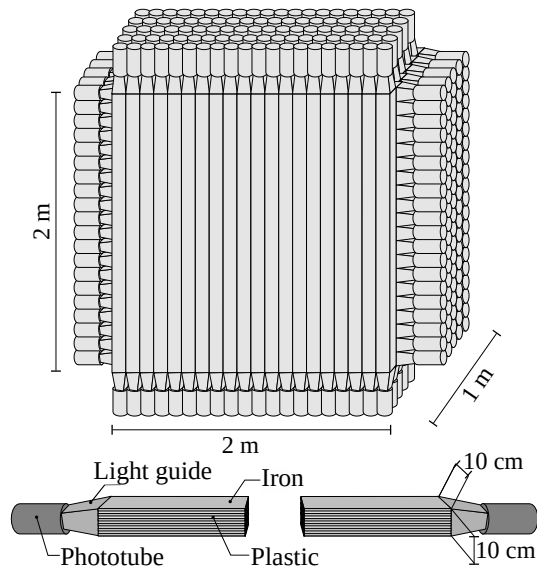


FIG. 2: Schematic views of the LAND detector without the veto wall and of the internal structure of a paddle.

The main part of LAND consists of ten consecutive planes, each plane containing twenty detector slabs, so-called paddles, with a length of 2 m and a cross section of  $10 \times 10$  cm<sup>2</sup>. The orientation of the paddles is alternating between vertical and horizontal, i.e. different for each pair of neighboring planes (Fig. 2). The paddles are made of alternating layers of plastic scintillator and iron converter sheets, all 5 mm thick, except for the front and rear

sheets of iron which are 2.5 mm thick. Photo-multiplier tubes mounted at both ends collect the light produced in all plastic layers of a paddle. The hit position within a paddle is determined from the ratio of amplitudes or from the time difference of the two signals recorded at either end. The intrinsic resolutions are 250 ps for the time and 3 cm for the position (rms values, Ref. [45]).

Global observables associated with a reaction event are generated by counting the total number of hits observed, called hit multiplicity, and by integrating the recorded pulse heights to obtain the total visible energy  $E_{\text{tot}}^{\text{vis}}$ . By using calibration parameters deduced from recorded cosmic-ray events, the visible energy can be expressed in MeV [6, 40]. Because of its depth of 1 m, the efficiency of LAND for detecting neutrons is high. According to the calibration obtained from the S107 experiment performed in 1992 with the fully functioning detector, neutrons of 600 MeV are detected with efficiency 0.94 [42, 43], a value in good agreement with recent Geant4 calculations [44]. The same level of performance was not reached in the present experiment with consequences discussed below (Sec. II G).

### C. High-efficiency volume

The neutron recognition in the LAND detector for the case of large neutron multiplicity and with the setup of the present experiment has been investigated in detail with results reported in Ref. [40]. As shown there, shadowing effects caused by the poles and yoke of the ALADIN magnet and the vacuum and detector chambers are visible in the hit distributions observed with LAND (cf. Fig. 6 in Ref. [40]). The expected azimuthal symmetry around the incoming-beam direction is observed up to lateral distances of about 70 cm. A more rapid decrease observed at vertical distances beyond 80 cm above or below the plane containing the beam axis coincides with the shadow of the poles of the ALADIN magnet and the magnet chamber as projected from the target position. The horizontal distribution extends further out in the direction away from the deflected beam. There, the projected shadow of the magnet is close to the end of the detector. Both distributions start to drop more rapidly at about 15 cm from the end of the detector. These edge effects are most likely caused by a reduced detection efficiency for the coincident signal at the far side of the paddle for hits located near one of the ends of a paddle.

With the aim to work with a homogeneous detection efficiency, a high-efficiency volume was defined within LAND and only events whose primary hits are located within this volume were accepted for further analysis. It had the form of a cube extending over the full length of LAND with the lateral dimensions

$$-150 < x < 0 \text{ cm}, -70 < y < 70 \text{ cm} \quad (1)$$

in the beam-oriented coordinate frame (the  $x$  direction points to the left,  $y$  up, and the  $z$  direction coincides

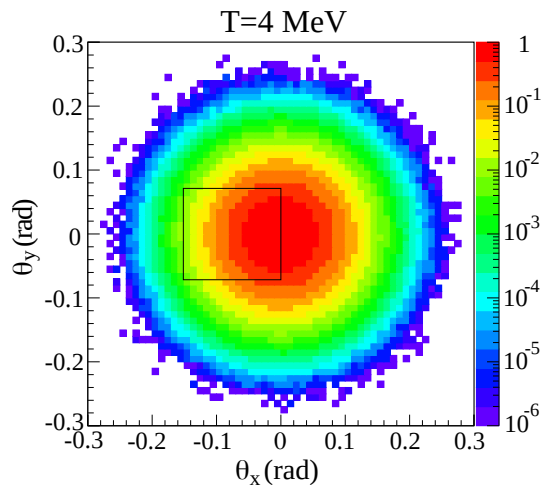


FIG. 3: Probability distribution with respect to the beam direction of the neutron intensity of a thermal source of temperature  $T = 4$  MeV, located at the target position and moving with the velocity of a projectile with 600 MeV/nucleon incident energy. The black square represents the high-efficiency area plotted in the chosen coordinate system in which the negative  $x$  direction viewed from the target position points to the right.

with the original direction of the incoming beam). The corresponding angular acceptance in the laboratory, as viewed from the target, is  $0^\circ$  to  $-8.72^\circ$  in horizontal and  $\pm 4.09^\circ$  in vertical directions at the entrance plane and  $0^\circ$  to  $-7.92^\circ$  and  $\pm 3.72^\circ$  at the rear plane of the high-efficiency volume.

#### D. Geant4 calculations

In addition to shadowing, neutron scattering by the various materials of the setup is expected to produce a neutron background downstream of the spectrometer and possibly hitting LAND. To determine its potential strength within the high-efficiency volume, a detailed study was performed within the Geant4 framework [41]. The interaction of neutrons with the detector itself is not taken into account in these calculations; only the conditions under which neutrons emitted from the target can approach the detector are examined. The model of the experimental setup consisted of replicas of the ALADIN magnet, the vacuum and detector chambers, and the time-of-flight wall, all with their accurate positions and dimensions but with a simplified geometry that omitted minor technical details.

The performed calculations fall into three classes. As a first step, pencil beams of neutrons with energies between 400 and 800 MeV were started from the target position, homogeneously distributed within a cone of polar angle  $\theta_{\text{lab}} \leq 15^\circ$ . Their trajectories and those of produced secondary particles were followed, if they were not absorbed earlier, until they passed through a test plane perpendicular

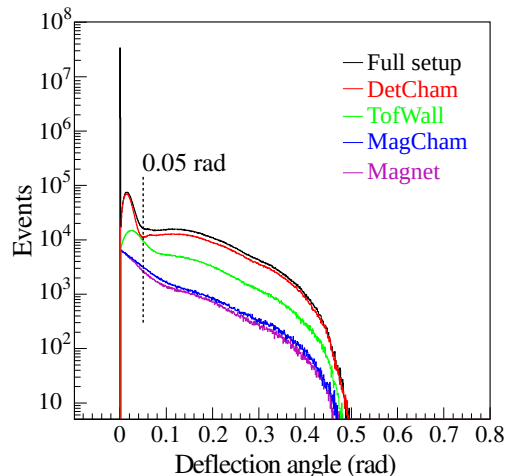


FIG. 4: Deflection angles of neutrons emitted in the direction of the high-efficiency area from a 4-MeV thermal source moving with beam velocity. The results are obtained from simulations for a source containing  $10^8$  neutrons in total with the full setup (black histogram) and with individual parts of the setup as indicated, specifically the magnet (magenta), the magnet chamber (MagCham in blue), the time-of-flight wall (TofWall in green), and the detector chamber (DetCham in red). The peak of non-interacting events, only shown for the full setup, contains  $3.56 \times 10^7$  events.

ular to the original beam direction at the location of the front plane of LAND.

Within this plane, a high-efficiency area was defined with the lateral dimensions of the high-efficiency volume. From the calculated results, the probabilities for reaching the test plane and the high-efficiency area without any or after specific scattering processes were determined. The results in graphical form are given in the Appendix.

For the second type of calculations, thermal sources of neutrons moving with beam velocity were placed at the target position and their histories up to the test plane followed in the calculations. The chosen temperatures  $T = 2 - 6$  MeV cover the interval of temperatures found for the identified spectator source of neutrons (see Sec. III C). The mere projection on the test plane of a source with temperature  $T = 4$  MeV, i.e. as obtained with all material removed, is shown in Fig. 3. The black square representing the high-efficiency area covers roughly one half of the central part of the source, sufficiently large to determine the main source properties in that case. More precisely, 42.4% of the particles of a source with 4 MeV temperature are emitted in the direction of the high-efficiency area, a value decreasing from 45% to 40% for sources with temperatures increasing from 3 MeV to 5 MeV.

The probability of scattering processes suffered by neutrons of a 4-MeV source is illustrated in Fig. 4 by showing the distribution of deflection angles representing the apparent change of the emission angle when viewing the displacement at the test plane from the target position. Deflection angles different from zero are caused by scat-

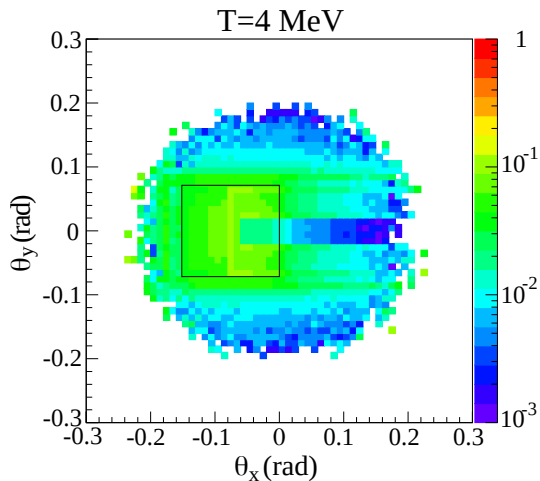


FIG. 5: Origin of scattered neutrons reaching the high-efficiency volume of LAND: the color code represents the probability for a neutron emitted with original direction  $(\theta_x, \theta_y)$  to enter the high-efficiency area of the test plane (black square) following a scattering process. The calculations are performed for a 4-MeV thermal source moving with beam velocity whose emission pattern is shown in Fig. 3.

tering processes experienced along the trajectories from the target to the test plane containing the front plane of LAND. For the figure, only the 42.4% of neutrons emitted in the direction of the high-efficiency area are considered. We find that very few are absorbed on the way, and that altogether 96% arrive at the test plane. A fraction of 87% of them reach the test plane in front of LAND unscattered as indicated by the peak at the origin in the distribution of deflection angles. The small bump at deflections up to 0.05 rad corresponding to  $\approx 3^\circ$  contains 5% of the neutrons arriving at the test plane, and only the remaining 8% suffer interactions leading to larger deflections from their original directions. The most probable deflection corresponding to the maximum of the bump at  $\approx 0.015$  rad is 15 cm at the test plane 9.78 m downstream. This is small relative to the dimensions of the high-efficiency area, and more than 70% of the scattered neutrons reach the high-efficiency area according to the calculations for the 4-MeV source.

The locations at which the interactions occur are indicated as well in Fig. 4. The colored histograms show the distributions of deflections obtained from calculations with virtual configurations containing only specific elements of the setup. Very few interactions in the magnet or in the magnet chamber are experienced by neutrons emitted toward the high-efficiency area. The contribution made by the time-of-flight wall is larger and exhibits the bump at small deflections. The main contribution originates from interactions in the exit flange of the detector chamber.

The distribution of the original directions of all scattered neutrons that finally pass through the high-efficiency area of the test plane are shown in Fig. 5. The

color code represents the probability of entering the high efficiency area for a neutron starting with a given direction  $(\theta_x, \theta_y)$ . Structure elements of the rear wall of the ALADIN detector chamber are clearly recognized. The narrow horizontal band with reduced scatter probability is caused by the thin exit window for the beam. It is 1.98-m wide, 28-cm high, made from 1-mm steel, and welded at beam height into a thicker exit flange mounted on the rear wall (Fig. 1). The rim structure of this flange is taken into account in the model of the experimental setup. It causes the vertical zone of higher scattering probability passing through the middle of the high-efficiency area at  $\theta_x \approx -0.08$  rad.

Neutrons which, without scattering, would miss the high efficiency area have a probability of about 1–2% to enter it, indicated by the light-blue color code outside the black square. Neutrons already starting toward the high-efficiency area have a probability of  $\approx 10\%$  to scatter and to still end up there, indicated by the mostly light green color code within the black square. The majority of them belongs to the group of neutrons forming the prominent bump with deflection angles of up to 0.05 rad (Fig. 4). The integrated yield as shown in Fig. 5 amounts to nearly 4% of the source intensity which, added to the 36% of neutrons reaching the high-efficiency area without interactions, yields  $\approx 40\%$  of the total source intensity. It is not far from the 42.4% originally emitted in directions contained in the high-efficiency area. However, the calculations also indicate that the scattered neutrons may lose energy in the process, forming a tail of lower intensity extending from the peak at beam rapidity to lower rapidities. Scattered neutrons are counted in the neutron multiplicities determined from the recorded total visible energy but may not be correctly placed in the rapidity and transverse-momentum distributions of the spectator source of neutrons.

The calculated rates of absorption, scattering, and background production are functions of the chosen source temperature but, for the relevant temperature interval, remain within 5–10% which indicates the general level of uncertainty caused by the interactions with the setup material. It may be summarized as a value of  $90 \pm 10\%$  for the ratio of neutrons reaching the high-efficiency volume of LAND versus the number of neutrons emitted toward it. Within this margin, the ALADIN-LAND setup appears to be well suited for the performed measurements.

A third type of calculations performed with nuclear beams had the aim of determining the level of a potential background of secondary neutrons produced by projectile fragments interacting with the material of the setup. The paths of selected types of fragments, starting from the target position and deflected by the magnetic field, were followed through the setup until they traversed the time-of-flight wall and the exit wall of the detector chamber. It was found that most of the secondary neutrons are emitted from a position near the end of the detector chamber and into narrow cones in directions close to that of the exiting beam. Their transverse momenta are insufficient

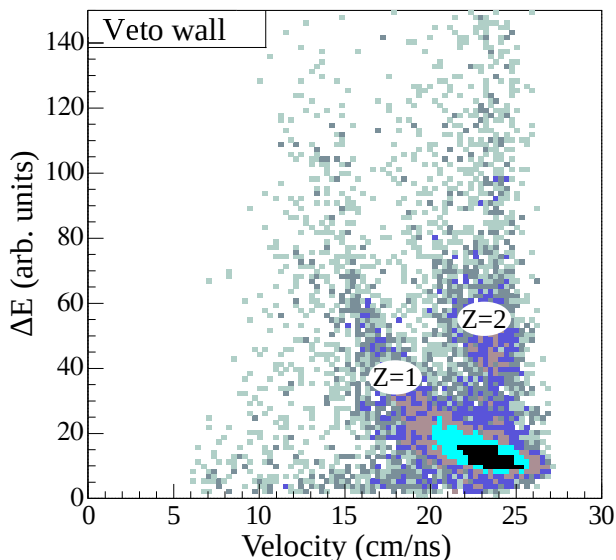


FIG. 6: Distribution of energy-loss signals  $\Delta E$  measured with the veto wall in front of the LAND detector as a function of the particle velocity. The registered charged particles are mainly protons with velocities close to the beam velocity of 23.8 cm/ns and depositing approximately 1.4 MeV in the detector.

to enter the high-efficiency volume of LAND with large probability. More details are given in the Appendix.

### E. Neutron identification and analysis

A cluster-recognition algorithm is used to identify individual particles within the hit distributions registered with LAND [40]. Charged particles are recognized by their energy loss signals deposited in the veto wall (Fig. 6). They consist of mainly hydrogen isotopes because heavier products emitted in forward direction into narrower angular cones do no longer reach LAND after having passed the ALADIN magnetic field. In the clustering procedures used for neutrons and charged particles, also the differences of their interaction with the LAND detector elements are taken into account. Neutrons produce secondary showers of ionizing particles in nuclear reactions with the detector material while charged particles, in addition, produce light signals by directly ionizing the plastic layers along their flight paths. Charged-particle hits are strongly correlated in time and space, consecutively following along the particle trajectory and possibly also ending in reaction showers similar to those generated by neutrons. According to their energy-loss in the detector material, 600-MeV protons do not penetrate deeper into LAND than through the first five planes while hits from neutron events are distributed throughout the full detector volume (Fig. 7).

The techniques used to analyze the LAND data are described in detail in Ref. [40], while here only the main analysis schemes are presented. The cluster analysis be-

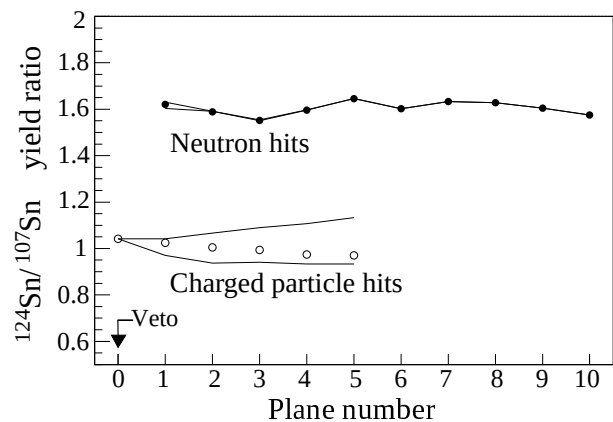


FIG. 7: Ratios of registered hit multiplicities for neutrons (filled circles) and charged particles (open circles) from reactions with  $^{124}\text{Sn}$  and  $^{107}\text{Sn}$  projectiles as a function of the LAND plane number. Plane 0 represents the veto wall. Solid lines correspond to upper and lower limits as obtained from the analysis (see text). They practically coincide for neutrons.

gins by identifying charged-particle clusters by their correlation with hits in the veto plane and by their consecutive appearance in the first few LAND planes. The remaining hits are attributed to neutron events. In the clustering procedure for neutrons, called the shower tracking algorithm (STA) in [40], hits are considered as correlated if they fall within a space and time window

$$\begin{aligned} -19 < \Delta x < 19 \text{ cm}, \\ -19 < \Delta y < 19 \text{ cm}, \\ -1 < \Delta t < 3 \text{ ns} \end{aligned} \quad (2)$$

but are not required to belong to consecutive planes. The search for clusters starts with the hits in the first plane and the search for a correlated hit in one of the following planes and is continued with the iterative search for further correlated members of the cluster. This procedure is then repeated by starting with remaining hits in the second LAND plane and continued until all clusters are identified.

The properties of a particle represented by a cluster of hits are determined by the position and time of the primary hit from which its velocity vector is calculated. With the time resolution of  $\Delta t \approx 650$  ps (FWHM), including the time spread resulting from the depth of the paddles, and flight paths of about 10 m, the velocity resolution is  $\Delta\beta/\beta \approx 1.6\%$ .

### F. Treatment of single hits

Not all hits are part of a cluster. When the clustering procedure is completed, a number of single hits may be left, isolated in space or time so that no correlation with other hits was found. They are partly single-hit neutron

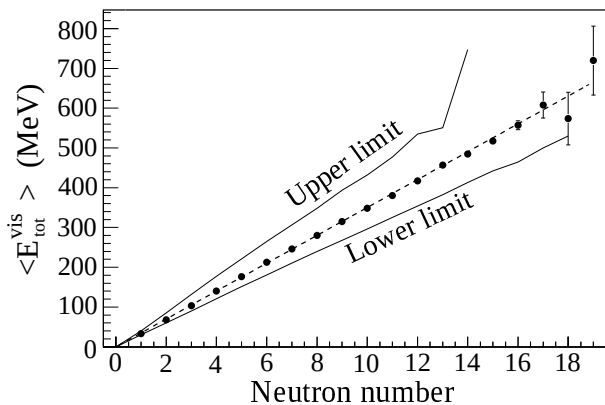


FIG. 8: The mean total visible energy  $\langle E_{\text{tot}}^{\text{vis}} \rangle$  as a function of the neutron number obtained from the AVE procedure (filled circles) for the case of  $^{124}\text{Sn}$  projectiles. Solid lines represent the upper and lower limits of  $\langle E_{\text{tot}}^{\text{vis}} \rangle$  as obtained with the MIN and MAX procedures, respectively. The dashed line corresponds to a mean value of  $\langle E_{\text{tot}}^{\text{vis}} \rangle = 35$  MeV per neutron.

events, as expected on the basis of the shower statistics, but may also result from the following technical inefficiencies:

- (1) Missing paddles: A small number of paddles ( $\approx 15\%$ ) were not properly functioning during the experiment. It may have the effect that unobserved hits cause the separation of larger clusters into two or more parts, thereby generating isolated hits.
- (2) Multiple hits: When two hits are registered in one paddle they are seen as one hit with a false position. Also its time is usually altered so that existing correlations may be destroyed.
- (3) A neutron may react with the LAND material at two or more locations distant from each other. These interactions will produce separate clusters or hits that are indistinguishable from patterns generated by two or more neutrons.

In order to assess the magnitudes of these effects, the data were analyzed with assumptions chosen to either maximize or minimize the number of resulting neutron events within reasonable limits (see Ref. [40] for a detailed description). Counting all single hits as neutron events produces an upper limit labeled “MAX” in the following. The number of single hits and thus of identified neutrons can be reduced by relaxing the requirements for a correlation given in Eq. (2). The results labeled “MIN” in the following were produced by requiring only the relaxed condition  $-7 < \Delta t < 4$  ns in time and none of the conditions in space. Similarly, conditions in between these extremes were used to generate a most likely result labeled “AVE” (for average).

The effects of the different analysis procedures cancel for some observables. Examples are the ratios of the multiplicities of hits assigned to neutron events as a function of the plane number for the reactions of  $^{124}\text{Sn}$  and  $^{107}\text{Sn}$  projectiles (Fig. 7). The ratios of proton hits were found to depend on the choice of the procedure because effects

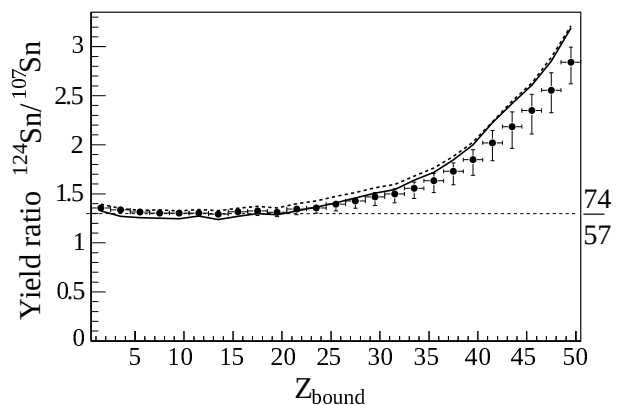


FIG. 9: The ratios of the mean visible energies  $\langle E_{\text{tot}}^{\text{vis}} \rangle$  (solid line), of the hit numbers  $N_{\text{hit}}$  (dashed line) and of the neutron numbers  $N$  from the clustering procedure (points) as obtained for reactions of the  $^{124}\text{Sn}$  and  $^{107}\text{Sn}$  projectiles as a function of  $Z_{\text{bound}}$ . The error bars represent the upper and lower limits obtained with the MIN and MAX procedures. The dashed horizontal line marks the ratio  $74/57 = 1.30$  of the neutron numbers of the two Sn projectiles.

(1) and (2) may also disturb the recognition of charged particles. The independence of the plane number is best realized with the AVE conditions.

The magnitude of the differences between the procedures is illustrated in Fig. 8. The total visible energy  $E_{\text{tot}}^{\text{vis}}$  obtained by integrating the recorded pulse heights should, on average, rise in proportion to the number of detected neutrons. The expected linearity is observed for each of the three procedures but the mean visible energy per neutron is considerably smaller for the MAX than for the MIN procedures. A mean value  $\langle E_{\text{tot}}^{\text{vis}} \rangle = 35$  MeV is obtained with the AVE procedure. An absolute calibration for this value at the time of the experiment does not exist for LAND. However, in the previous experiment S107, tagged neutrons from the breakup of deuteron beams at various energies were used to study the response of the detector to single neutrons [42, 43]. With this data set, multi-neutron events were generated with the technique of event mixing and, subsequently, analyzed with the present clustering procedures [40]. The most satisfactory results were obtained with the AVE procedure, which was therefore adopted as the most realistic choice.

As a further test, we show in Fig. 9 the ratios of the measured mean visible energies  $\langle E_{\text{tot}}^{\text{vis}} \rangle$ , of the hit numbers  $N_{\text{hit}}$ , and of the neutron numbers  $N$  from the three clustering procedures as obtained from the two reactions with  $^{124}\text{Sn}$  and  $^{107}\text{Sn}$  projectiles as a function of  $Z_{\text{bound}}$ . In the limit of small  $Z_{\text{bound}}$ , i.e., large excitation energies, this ratio approaches the value  $74/57 = 1.30$ , i.e. the ratio of the neutron numbers of the two projectiles, and the ratios of all three observables coincide. On the opposite side, for large  $Z_{\text{bound}}$ , the evaporation from excited projectile residues is the dominant source of neutrons. Considerably more neutrons are emitted from the neutron-rich  $^{124}\text{Sn}$  than from the neutron-poor  $^{107}\text{Sn}$  residues.

It explains why the  $Z_{\text{bound}}$  averaged ratio 1.6 shown in Fig. 7 is larger than 74/57. For large  $Z_{\text{bound}}$ , the ratio of the neutron numbers determined with the clustering procedure is lower by up to 10% than those of the global observables  $\langle E_{\text{tot}}^{\text{vis}} \rangle$  and  $N_{\text{hit}}$ .

### G. LAND efficiency

A calibration of the LAND efficiency for neutrons at the time of the experiment does not exist. As the data analysis indicates, the performance of the detector had been slightly degraded. About 15% of the paddles were not functioning properly, mainly in the rear part of the detector. More importantly, the thresholds for registering hits had increased. The analysis of the measured hit distribution for one-neutron events in comparison with the S107 results obtained with the fully functional detector led to the conclusion that the hit-registration probability had decreased to approximately one half of its original value [40]. The corresponding detection efficiency for one-neutron events was estimated as only 73%.

The obtained value, however, did not take into account that the breaking of clusters by unobserved hits into two or more separate parts, mostly single hits, may increase the neutron multiplicity returned by the applied clustering algorithm. In that respect, it may be considered a lower limit, similar to the MIN choice in STA discussed in Sec. IIF and represented by the upper limit displayed in Fig. 8. The alternative AVE choice, yielding multiplicities larger by a factor  $\approx 1.25$  than the MIN option, was found to best account for the actual inefficiencies of LAND and to lead to reliable multiplicity estimates in simulations using actual spatial and temporal hit distributions measured in the present experiment (cf. Fig. 3 in [40]). The resulting most probable detection efficiency at the time of the experiment thus amounts to  $0.73 \times 1.25 \approx 0.9$ .

There is even a tendency, in particular for the larger multiplicities 5 to 15 encountered here, for a slight overestimation of the order of one up to two neutrons, corresponding to 10% to 20% in this range of multiplicities. The effect persists in simulations modeling properties of LAND at the time of the experiment (cf. Fig. 5 in [40]). By its magnitude, it may even partly compensate for the losses caused by the finite LAND efficiency of 0.9. We therefore adopt the results obtained with the AVE conditions without further corrections as the most realistic choice for the present experiment.

The uncertainty of this procedure is clearly significant. Even if the MIN and MAX procedures are rejected as extreme options, it may still be estimated to be of the order of  $\pm 15\%$ . Together with the probability of  $90 \pm 10\%$  for neutrons reaching the high-efficiency volume of LAND (Sec. IID), we arrive at a value of  $0.9 \pm 0.2$  for the overall detection efficiency applicable to this experiment. As a common factor, it only mildly affects relative results obtained in comparing the studied reactions (cf. Fig. 9).

## III. EXPERIMENTAL RESULTS

### A. Reaction characteristics

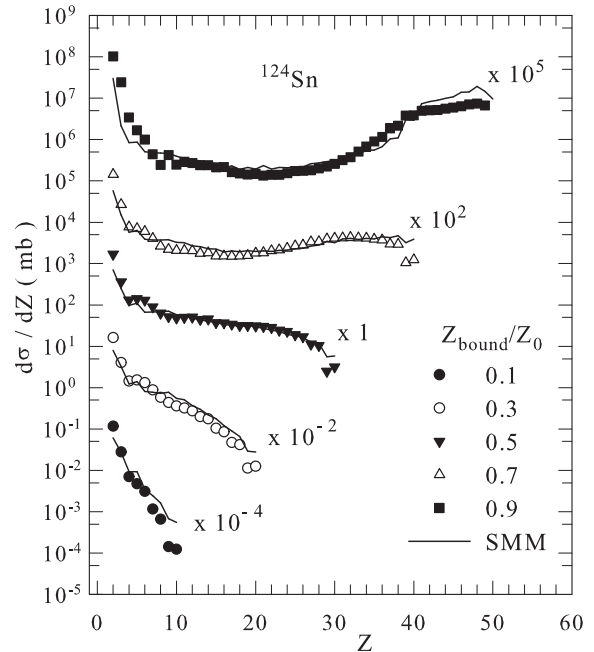


FIG. 10: Experimental cross sections  $d\sigma/dZ$  for the fragment production following collisions of  $^{124}\text{Sn}$  projectiles with a natural Sn target at 600 MeV/nucleon, sorted into five intervals of  $Z_{\text{bound}}/Z_0$  with centers as indicated and width 0.2 (symbols) in comparison with normalized SMM calculations (lines).  $Z_0 = 50$  represents the atomic number of the  $^{124}\text{Sn}$  projectiles. The scale factors used for displaying the cross sections are indicated (reprinted with permission from Ref. [2]; Copyright © 2011 by the American Physical Society).

As an introduction, two figures will be used to briefly characterize the studied reactions. The fragmentation of the projectile spectators after the initial stage of the collision was investigated in detail in Ref. [2]. As an example taken from this work, the experimental cross sections  $d\sigma/dZ$  for the fragment production following collisions of  $^{124}\text{Sn}$  projectiles are shown in Fig. 10, sorted into five intervals of  $Z_{\text{bound}}$ . The charge distributions evolve from a so-called 'U-shaped' distribution at large impact parameters, with the production of heavy residues and light fragments in asymmetric binary decays, through a power-law shaped to a rapidly dropping exponential spectrum in the bin of smallest impact parameter. This evolution is a well-known and characteristic phenomenon and expected as a manifestation of the nuclear liquid-gas phase transition [3, 39, 46–48]. The thin lines in the figure represent the results of SMM calculations as described in Ref. [2]. A comparable reproduction of the charge correlations characterizing the projectile fragmentation at the present energy was achieved with the dynamical isospin quantum molecular dynamics (IQMD) transport

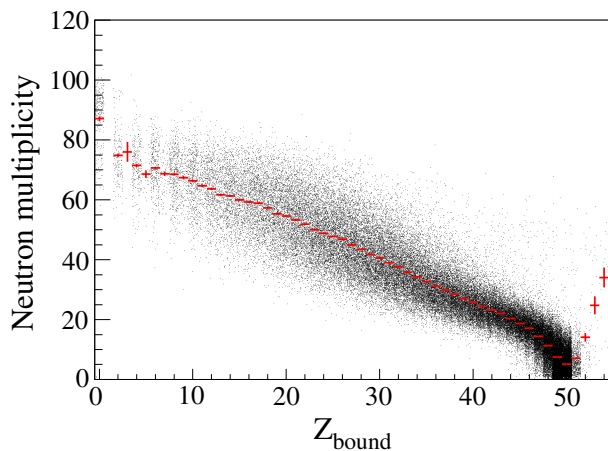


FIG. 11: Neutron multiplicity as a function of  $Z_{\text{bound}}$  according to the Bertini cascade implemented in Geant4 for the reaction  $^{124}\text{Sn} + \text{Sn}$  at 600 MeV/nucleon. A condition  $E_{\text{lab}} > 100$  MeV for neutrons to be counted is imposed. The short-dashed line (red) follows the mean values of the so obtained multiplicity for given  $Z_{\text{bound}}$ .

model [22].

The neutron multiplicities expected for these processes are shown in Fig. 11 as a function of  $Z_{\text{bound}}$ . The predictions were obtained with the Bertini cascade model as implemented in the Geant4 toolkit [49]. Besides the initial intranuclear cascade with excitons, the model treats preequilibrium emissions, Fermi breakup for excited nuclei with  $A < 12$  and  $Z < 6$ , and fission and evaporation from the produced spectator nuclei. The calculations were performed by simply directing a beam of  $^{124}\text{Sn}$  projectiles on a Sn target of thickness 0.5 mm within the Geant framework without taking any properties of the setup into account. Only neutrons with kinetic energies exceeding  $E_{\text{lab}} = 100$  MeV were counted, a condition meant to exclude neutrons from secondary deexcitations of target fragments. The odd-even structure at small  $Z_{\text{bound}}$  follows from the fact that  $Z_{\text{bound}}$ , by definition, cannot be equal to 1 and that events containing a single light fragment of odd  $Z$  without accompanying  $\alpha$  particles are apparently rare. The odd-even structure is also visible in the measured reaction cross sections [2].

The calculated reaction cross section  $\sigma_{\text{react}} = 4.52$  b compares well with the value measured in the experiment [2]. In peripheral collisions, the calculated neutron multiplicities reach rapidly values near 20 from where they increase smoothly with decreasing  $Z_{\text{bound}}$  to values close to 80 for the number of free neutrons in the most central collisions. This latter number is consistent with expectations based on the measured composition of the light-particle source in central collisions. For the  $^{197}\text{Au} + ^{197}\text{Au}$  reaction at 400 MeV/nucleon, the relative yields of  $p:d:t:^3\text{He}:^4\text{He}$  were found to be 1:0.65:0.4:0.2:0.2, as measured by the FOPI Collaboration [50]. Neglecting heavier fragments and assuming the same composition for the  $^{124}\text{Sn} + \text{Sn}$  system, with a very similar  $N/Z$  but at the

higher energy 600 MeV/nucleon, leads to a composition containing 35 free protons, 65 protons and 72 neutrons bound in light charged particles, and 76 free neutrons. However, very few of these fireball neutrons are likely to be emitted into the small solid angle in forward direction covered by LAND.

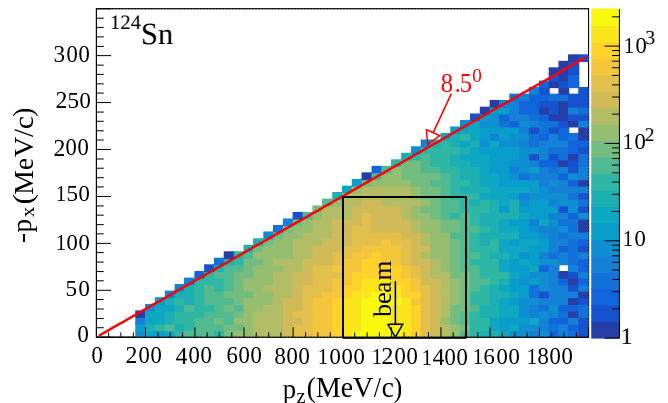


FIG. 12: Distribution of identified neutrons in the plane of transverse momentum  $-p_x$  versus longitudinal momentum  $p_z$  for the fragmentation of  $^{124}\text{Sn}$  projectiles in collisions with natural Sn targets at 600 MeV/nucleon incident energy. The full line (red) indicates the acceptance cut in the analysis. The black rectangle indicates the two-dimensional interval  $|p_x| \leq 150$  MeV/c and  $1000 \leq p_z \leq 1500$  MeV/c used for the determination of the source temperature and multiplicity.

As will be shown below, the multiplicity of the spectator source of neutrons identified with LAND reaches its maximum for  $Z_{\text{bound}} \approx 35$  with values around 11 for the  $^{124}\text{Sn}$  projectile whereas it is around 30 – 35 according to the Bertini model (Fig. 11). It is clear that, at the corresponding intermediate impact parameters, the intensity of the fireball is still significant but the number of free neutrons may also be somewhat overestimated with the Bertini model, possibly by up to 10 – 15 neutrons. In this range of  $Z_{\text{bound}}$ , the multiplicity of intermediate mass fragments is still around one or larger [2], and the observed charge spectrum stretches up to the evaporation regime around  $Z = 30$  (Fig. 10). This type of multifragmentation process with neutrons bound in heavier fragments is not explicitly accounted for in the model. The calculations, nevertheless, indicate that the total number of free neutrons emitted in mid-peripheral collisions with  $Z_{\text{bound}} \geq 35$  and particularly also at peripheral collisions with  $Z_{\text{bound}}$  up to nearly 50 is larger than that of the spectator neutron source experimentally observed at forward angles.

## B. Spectator source of neutrons

Longitudinal momenta were determined from the neutron time-of-flight measured with a resolution of  $\Delta t \approx 650$  ps (FWHM), corresponding to  $\Delta p_z \approx 50$  MeV/c or about 4% for beam velocity neutrons. The accepted

range of perpendicular momentum is largest in the horizontal direction but only on the side opposite to the deflected beam (cf. Figs. 1 and 3), and is shown for  $^{124}\text{Sn}$  projectiles in Fig. 12. The spectator source is clearly visible and is centered at momenta slightly below the projectile momentum  $p_{\text{proj}} = 1216 \text{ MeV}/c$  per nucleon. The interval in the plane of momenta  $p_x$  vs  $p_z$  used for determining the magnitude and apparent temperature of the neutron source is indicated. For the transverse dimension, an upper limit  $-p_x \leq 150 \text{ MeV}/c$  was chosen which keeps the analysis interval within the high-efficiency volume for longitudinal momenta  $p_z \geq 1000 \text{ MeV}/c$ . The rapid drop of the source intensity in the interval  $50 \leq |p_x| \leq 100 \text{ MeV}/c$  confirms that also in the vertical dimension the dominant part of the spectator neutron source is accepted within the high-efficiency volume with  $|p_y| \leq 87 \text{ MeV}/c$  for beam-velocity neutrons.

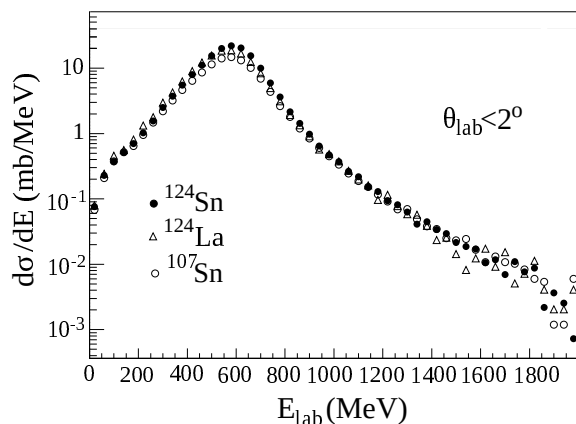


FIG. 13: Inclusive differential cross section of neutrons in the laboratory detected within the solid angle  $\theta_{\text{lab}} < 2^\circ$  for the three projectiles as indicated. No corrections are applied to the recorded data (cf. Sec. II G).

Absolute cross sections were obtained with the normalization determined for this experiment [2]. Differential production cross sections measured for neutrons within a cone  $\theta_{\text{lab}} < 2^\circ$  at very forward angles and integrated over the range of  $Z_{\text{bound}} \geq 2$  up to the projectile  $Z$  are shown in Fig. 13. The choice of  $\theta_{\text{lab}} < 2^\circ$ , much narrower than the acceptance of LAND in this experiment, was made to get close to the geometry of the Berkeley experiments of Madey *et al.* [17–19], and to permit the comparison with their results (see Sec. V A).

Here and in the following, no corrections are applied to the recorded data because precise correction factors were not obtained. According to the results presented in Sec. II D, the possible losses of neutrons between the target and the detector are of the order of  $10 \pm 10\%$ , somewhat depending on the angular distribution of the emitted neutrons. The LAND efficiency, on the other hand, is close to unity but is somewhat dependent on the event multiplicity (Sec. II G). According to the deduced overall detection efficiency  $0.9 \pm 0.2$ , the recorded cross sections and mean multiplicities are possibly too

low by about 10% but are affected with uncertainties up to  $\pm 20\%$ .

The spectra reach their maxima at laboratory energies 560 to 600 MeV and drop off rapidly toward higher and lower energies. In a thermal interpretation, their widths indicate temperatures of 4.5 to 5 MeV for the emitting sources, not taking into account a possible broadening caused by a finite distribution of the longitudinal velocities of the spectator sources. For reasons discussed below, the HWHM on the high-energy side was used for this estimate. The double differential cross section reaches a peak value  $d\sigma/d\Omega/dE = 5.5 \times 10^3 \text{ mb/sr/MeV}$  for  $^{124}\text{Sn}$  fragmentations and values smaller by about 30% and 40% for the cases of  $^{124}\text{La}$  and  $^{107}\text{Sn}$ , respectively. These differences are, again, larger than the relative differences of the neutron numbers of the three projectiles (cf. Figs. 7 and 9).

### C. Thermal properties

The momentum distributions and energy spectra shown in Figs. 12 and 13 suggest that the neutron emission from the spectator source has thermal characteristics with Maxwellian distributions in the projectile frame. This is expected for neutrons evaporated from heavy projectile residues and should mainly reflect the internal temperature of the emitting fragment. The effects of recoil and of the motion of the emitting source in the projectile rest frame are very small in this case. The momentum transfer to the projectile residues is not discussed in Ref. [2] but existing preliminary analyses indicate that it is very similar to those reported for Au and Pb fragmentations in Refs. [32, 51, 52]. It adds to the momenta of neutrons emitted from lighter fragments. In the simplest approximation, its contribution to the observed neutron temperature may be estimated as  $T_f/A_f$  with  $T_f$  being the temperature describing the fragment motion in the projectile rest frame and  $A_f$  the mass number of the emitting fragment. With  $T_f \approx 15 \text{ MeV}$  as deduced in Ref. [32], this contribution is indeed very small for emissions from heavy residues but may reach values of the order of MeV for emissions from lighter fragments. The resulting temperatures should thus be considered as effective temperatures of the projectile neutron source.

Because of their superior momentum resolution, the transverse components  $p_x$  and  $p_y$  were chosen for the following analysis. The neutron density distribution in the  $p_y$  vs  $p_x$  plane is assumed to be given by

$$\frac{\partial^2 N}{\partial p_x \partial p_y} = N_S G_T(p_x) G_T(p_y) + N_B \beta(p_x, p_y) \quad (3)$$

where  $N_S$  is the measured neutron multiplicity, and  $G_T$  is a classical Maxwellian function of the form

$$G_T(p_i) = \frac{1}{\sqrt{2\pi mT}} \exp\left(-\frac{p_i^2}{2mT}\right), \quad i = x, y \quad (4)$$

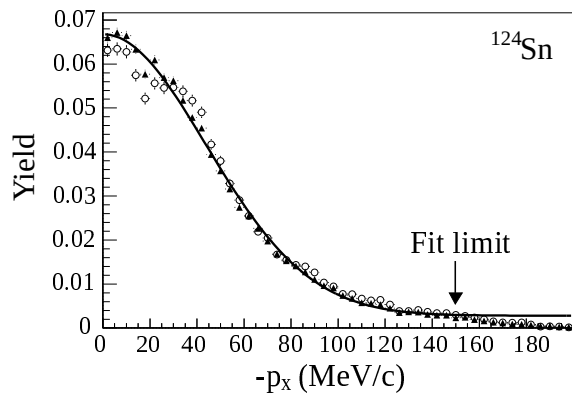


FIG. 14: Distribution of transverse momentum  $-p_x$  for neutrons from the fragmentation of  $^{124}\text{Sn}$  projectiles, selected with the condition  $Z_{\text{bound}} \geq 45$ . The open circles and the filled triangles represent the normalized yields of primary hits within a neutron cluster and of all hits, respectively. The result of a fit with a Gaussian distribution corresponding to  $T = 2.04$  MeV superimposed on a constant background is represented by the solid line. The fit limit at  $p_x = -150$  MeV/ $c$  is indicated.

with neutron mass  $m$  and temperature parameter  $T$ . A potentially existing neutron background is taken into account with the added background term in Eq. (3). Here  $N_B$  is the total number of background neutrons and  $\beta(p_x, p_y)$  is a background distribution function, normalized to unity. This function is not known, however, and has been assumed to be approximately constant over the region dominated by the emission from the projectile spectators. The goal is to determine the three parameters temperature  $T$ , source neutron multiplicity  $N_S$ , and the background neutron multiplicity  $N_B$ .

To find the temperature parameter  $T$ , the distribution of one of the particle momentum components is fitted with a Gaussian function added to a constant background pedestal:

$$f(p_x) = C_1 \exp\left(-\frac{p_x^2}{2\sigma^2}\right) + C_2 \quad (5)$$

where  $C_1$ ,  $C_2$  and  $\sigma$  are the fitted parameters. The comparison with Eq. (4) gives a correspondence between the  $\sigma$  parameter and the temperature:  $\sigma = \sqrt{mT}$ .

The transverse-momentum spectra for  $|p_x| \leq 150$  MeV/ $c$  are indeed well described by Gaussian fits superimposed on a constant pedestal that may represent neutrons from a source with wider momentum distributions together with a background of scattered neutrons. An example of the results obtained for the fragmentation of  $^{124}\text{Sn}$  projectiles is shown in Fig. 14. In the chosen rather peripheral case with  $Z_{\text{bound}} \geq 45$ , neutrons can be assumed to be mainly emitted from excited residues (cf. Fig. 10). The background level is evidently very low, consistent with the expectation that scattering processes may cause the flight times to be longer and to

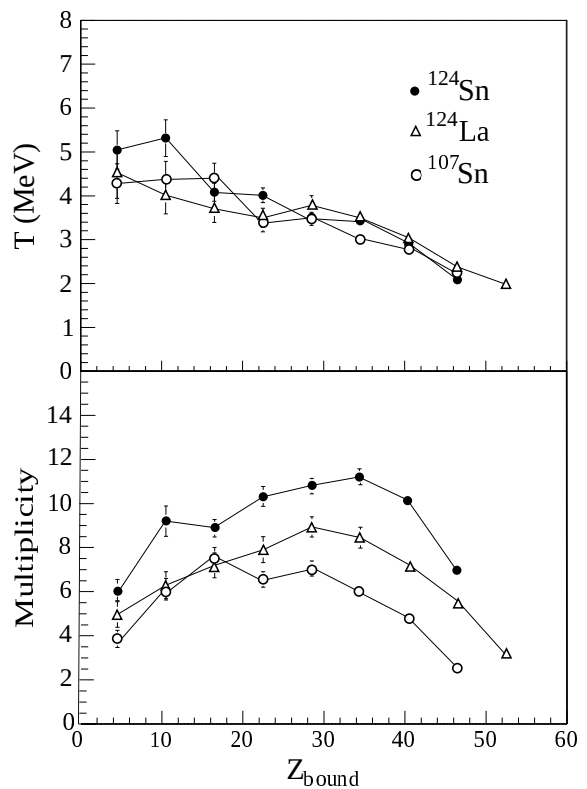


FIG. 15: Top: temperature parameter of the projectile source as a function of  $Z_{\text{bound}}$  for  $^{124}\text{Sn}$  (filled circles),  $^{124}\text{La}$  (triangles), and  $^{107}\text{Sn}$  (open circles) projectiles. Bottom: multiplicity of neutrons emitted from the projectile source as a function of  $Z_{\text{bound}}$  for the same three cases. The vertical bars in both panels include the errors returned by the fitting routine but not the overall uncertainty of the obtained multiplicities. No corrections are applied to the recorded data (cf. Sec. II G).

partly fall outside the chosen interval corresponding to  $p_z > 1000$  MeV/ $c$ . The fit limit  $-p_x \leq 150$  MeV/ $c$  is equal to the upper limit of the analysis interval (Fig. 12).

The temperatures determined with this method are shown in Fig. 15 (top) as a function of  $Z_{\text{bound}}$ . They are found to be quite similar for all three reactions, smoothly increasing from about 2 MeV at large  $Z_{\text{bound}}$  to values between 4 and 5 MeV for the most central collisions recorded in this experiment, there with uncertainties of up to 0.5 MeV. Part of this rise may be related to the source motion and recoil effects discussed above. Over the full range of  $Z_{\text{bound}}$ , the neutron temperatures are lower by typically about 2 MeV than the chemical breakup temperatures of 4 to 8 MeV determined for the present reactions [1]. For  $Z_{\text{bound}} = 20 - 30$ , the interval for which the multiplicity of intermediate-mass fragments reaches its maximum (cf. Fig. 10), the neutron temperatures are between  $T = 3.5$  and 4.0 MeV while the chemical breakup temperature is  $T \approx 6$  MeV (Fig. 16).

Lower temperatures are expected as average values in the case of deexcitation cascades that lead to the ground states of the emitting fragmentation products. However,

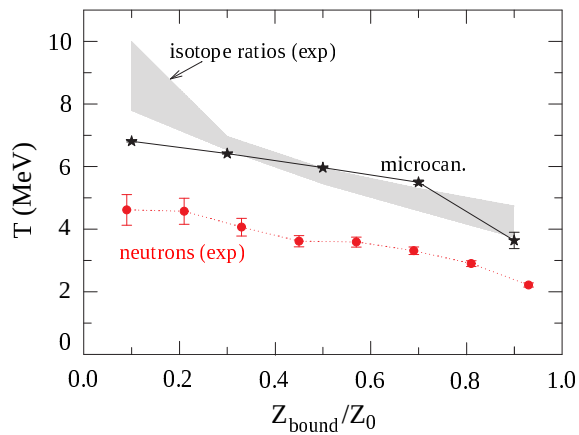


FIG. 16: Average temperature of the neutron sources of the three systems, determined from the measured momentum distributions, as a function of  $Z_{\text{bound}}$ , normalized with respect to the projectile atomic number  $Z_0$ , (filled circles in red) in comparison with the mean microcanonical temperature of the SMM description, calculated with a symmetry coefficient  $\gamma = 14$  MeV and averaged over the three projectile ensembles (stars in black). The average individual errors for the three systems are shown where they are larger than the symbols. The lines are meant to guide the eye. The shaded band represents the experimental isotope temperatures reported in Ref. [1], including the spread of the six values of the  $T_{\text{HeLi}}$  and  $T_{\text{BeLi}}$  temperatures for the three systems (figure adapted from Ref. [2]).

a similar reduction has not been observed for the evaporation component identified in proton spectra measured for  $^{197}\text{Au}$  fragmentations at 1000 MeV/nucleon [9]. The proton temperature  $T_p \approx 6$  MeV in the range of maximum fragment production is similar to the double-isotope temperatures determined for these reactions [8, 53, 54]. For  $\alpha$  particles from the same reaction, an evaporation component with  $T_\alpha = 5 \pm 2$  MeV has been identified in the measured kinetic energy spectra [54]. In spite of the partly large errors, the observed temperatures of evaporation-type light particles seem compatible with an interpretation identifying them as properties of secondary emissions with neutrons dominating in the later stages.

#### D. Integrated neutron yields

By integrating over the three-dimensional isotropic Gaussian source with the width parameter determined from the  $p_x$  spectra, the multiplicities, i.e. the number of neutrons emitted from the projectile-spectator source, were obtained. These neutron multiplicities as a function of  $Z_{\text{bound}}$  are shown in the bottom panel of Fig. 15. They exhibit broad maxima in the  $Z_{\text{bound}}$  interval of approximately 20 to 40. For larger  $Z_{\text{bound}}$  the excitation energies appear to be lower, so that the neutron emission drops accordingly. For smaller  $Z_{\text{bound}}$ , the excitation energy per nucleon may be larger but the source size becomes

smaller as a result of the more central impact parameter. At small  $Z_{\text{bound}}$ , the neutron multiplicities correspond to the  $N/Z$  ratio of the projectile. They are, on average, 30% higher for the case of  $^{124}\text{Sn}$  than for the two neutron-poor projectiles, a value close to their difference in  $N/Z$  as already indicated in Fig. 9. In more peripheral collisions, for  $Z_{\text{bound}} > 25$ , the neutron multiplicities exhibit a strong dependence on the neutron content of the incoming projectiles, stronger than in proportion to their total neutron numbers which are equal to effectively 57.7, 67.5, and to 74 for the three cases. However, after normalization with respect to the mass number  $A_0$  of the projectile and plotted as a function of  $Z_{\text{bound}}/Z_0$ , the multiplicities of the two neutron poor systems describe a common curve (cf. Ref. [34]).

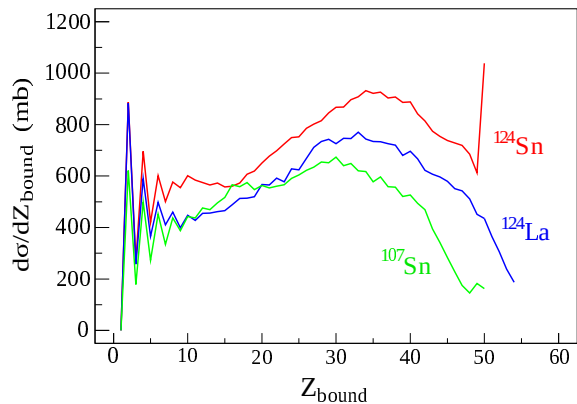


FIG. 17: Production cross sections of the identified spectator source of neutrons as a function of  $Z_{\text{bound}}$  for the three projectiles  $^{124}\text{Sn}$ ,  $^{124}\text{La}$ , and  $^{107}\text{Sn}$  (see text for the uncertainties).

Production cross sections of the identified spectator neutron source were obtained by multiplying the multiplicities with the measured event cross sections shown in Fig. 4 of Ref. [2]. For that purpose, the multiplicities were linearly interpolated, and slightly extrapolated at both ends, to obtain a smooth variation with  $Z_{\text{bound}}$ . The results are shown in Fig. 17. At small  $Z_{\text{bound}}$ , the cross sections exhibit the alternating structure caused by the definition of  $Z_{\text{bound}}$  as explained above and in Ref. [2]. With increasing  $Z_{\text{bound}}$ , they essentially reflect the differences of the multiplicities. The  $Z_{\text{bound}}$ -integrated cross sections are large and amount to 35 b for  $^{124}\text{Sn}$  and 30 and 24 b for the neutron poor  $^{124}\text{La}$  and  $^{107}\text{Sn}$ , respectively. These values are affected with the overall uncertainty of the measured neutron multiplicities (Sec. II G) and by the inefficiencies of the experimental trigger at large  $Z_{\text{bound}}$  discussed in Ref. [2].

## IV. STATISTICAL ANALYSIS

### A. Ensemble calculations

The statistical interpretation of the fragmentation processes observed in the present reactions was performed within the statistical multifragmentation model (SMM, Ref. [3]) and reported in Ref. [2]. The statistical breakup and decay were calculated for parametrized ensembles of excited sources representing the variety of excited spectator nuclei expected in a participant-spectator scenario. Following the scheme developed in Ref. [7], the parameters of the ensemble were determined empirically by searching for an optimum reproduction of the measured fragment charge distributions and correlations. As an example, the experimental charge distributions, measured for  $^{124}\text{Sn}$  and shown in Fig. 10, are well reproduced. Equally good descriptions have been achieved for the cases of  $^{107}\text{Sn}$  and  $^{124}\text{La}$  projectiles [2].

The microcanonical temperatures obtained for the disintegrating sources were found to coincide with the double-isotope-yield temperatures deduced from He, Li, and Be fragment yields [1] as shown in Fig. 16. Effects of the parameters of the liquid-drop description of produced fragments were investigated as well. In particular, the coefficient  $\gamma$  of the symmetry term had to be modified, so as to provide an adequate description of the measured isotopic distributions of fragments with  $Z \leq 10$ .

### B. Neutron multiplicities and temperatures

The SMM predictions for the mean neutron multiplicity as a function of  $Z_{\text{bound}}$  are shown in Fig. 18. They exhibit the observed global behavior with maxima appearing at intermediate  $Z_{\text{bound}}$  but are below the experimental values at small  $Z_{\text{bound}}$ . At large  $Z_{\text{bound}}$ , in the regime from U-shaped to power-law spectra (Fig. 10), the experimental multiplicities are reproduced rather well. In addition, a significant sensitivity to the coefficient  $\gamma$  chosen for the symmetry term in the liquid-drop description of the produced fragments is observed, most prominently for the case of the neutron-rich  $^{124}\text{Sn}$ . The comparison is consistent with the observation that a reduced value for  $\gamma$  is required for successfully reproducing the yields of neutron rich fragments [2]. A more precise determination of  $\gamma$  is precluded by the overall uncertainty  $\pm 20\%$  of the experimental neutron multiplicities (Sec. II G).

According to the calculations, the produced neutrons are mainly originating from the secondary decay of excited fragments as illustrated in Fig. 19. The relative intensities of neutrons created in the primary partitioning of the excited sources are very small with  $Z_{\text{bound}}$ -integrated strengths between 3.5% and 4.5% of the total yields. Their rise-and-fall behavior with a broad maximum centered at  $Z_{\text{bound}}/Z_0 = 0.5$  is similar to that of intermediate-mass fragments.

The yield of neutrons from secondary emissions is

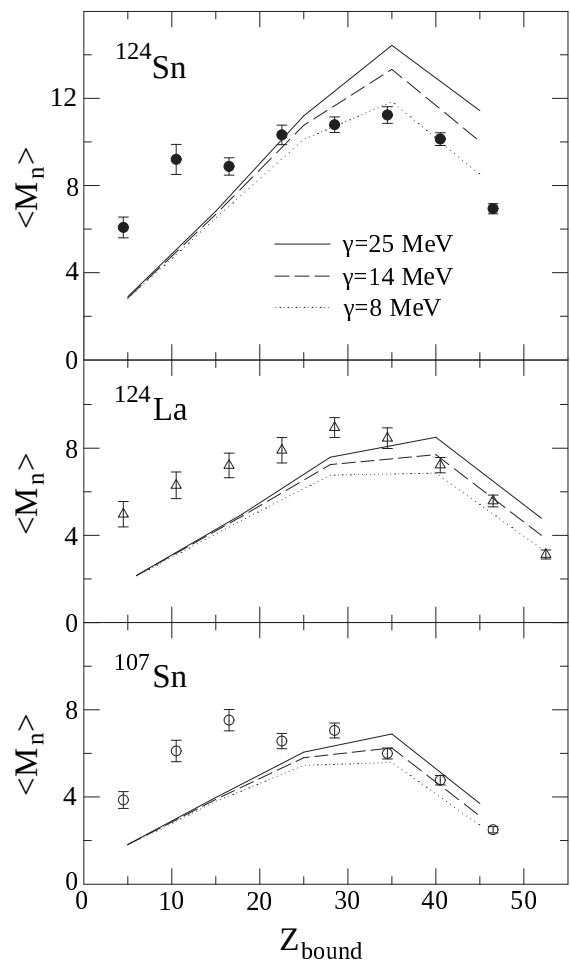


FIG. 18: Mean neutron multiplicity  $\langle M_n \rangle$  of the spectator sources produced in the fragmentation of  $^{124}\text{Sn}$  (top panel),  $^{124}\text{La}$  (middle panel), and  $^{107}\text{Sn}$  (bottom panel) as a function of  $Z_{\text{bound}}$ . The experimental data, presented in Fig. 15, are given by the symbols. The results of the SMM ensemble calculations, shown for values of the symmetry energy coefficient  $\gamma = 25, 14,$  and  $8$  MeV, are represented by the full, dashed, and dotted lines as indicated. The displayed experimental errors do not include the overall uncertainty discussed in Sec. II G.

clearly dominant but the predicted  $Z_{\text{bound}}$  dependence is only partly in agreement with the experimental data. In particular, at large  $Z_{\text{bound}}$ , the neutron yields are overestimated. One of the possible explanations for this discrepancy is related to the fact that the ensembles of sources were adjusted to reproduce the observed fragment yields and correlations. The fragment yields are low at both ends of the  $Z_{\text{bound}}$  spectrum with the effect that the ensemble parameters are only poorly constrained. A closer inspection of the predicted fragment yields shows that, e.g., the production of heavy residues with  $Z \geq 40$  in the bin of largest  $Z_{\text{bound}}$  is overestimated by a factor of perhaps 2 (Fig. 10 and Figs. 4 and 10-12 in Ref. [2]). It may contribute significantly to the neutron yields.

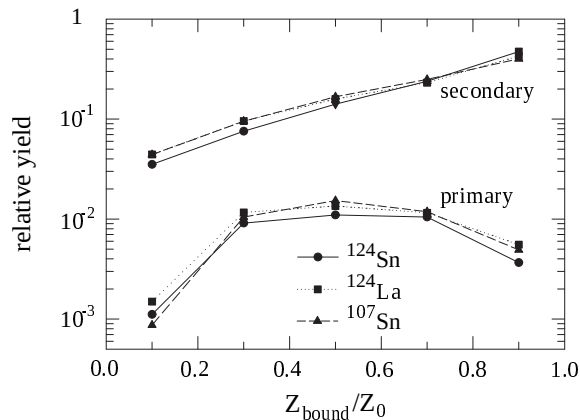


FIG. 19: The SMM result for the relative yield of produced neutrons separated into the groups of neutrons from the primary disintegration of the ensemble of excited sources (primary) and from the secondary deexcitation of fragmentation products (secondary) as a function of  $Z_{\text{bound}}/Z_0$  for the three reactions as indicated. The three cases are each individually normalized. The lines connect the data symbols.

A second argument, addressing the underprediction of neutrons at smaller  $Z_{\text{bound}}$ , may be related to the crescent-shaped geometry expected for the spectator systems emerging from collisions with small impact parameter. They may be only weakly connected and disintegrate into several smaller entities before they equilibrate [55]. Neutrons loosely attached to these structures may not participate in the statistical processes forming the sources accounting for the small number of fragments that are observed. Also in that case, fragment yields alone are not sufficient for a realistic description of the more complicated structure of the spectator system. One may, therefore, conclude that not only the neutron multiplicity at small impact parameter is underpredicted for that reason but also the relative strength of the primary group of neutrons (Fig. 19). There is no doubt, however, that secondary processes dominate at intermediate to large impact parameters.

For the reasons just discussed, the bins of large and small  $Z_{\text{bound}}$  are not included in the evaluation of the temperatures characterizing the source of neutrons modeled with the SMM. The distributions of all neutrons integrated over the interval  $10 \leq Z_{\text{bound}} \leq 40$  exhibit temperature values  $T = 4.5, 4.4,$  and  $4.7$  MeV for the fragmentations of  $^{124}\text{Sn}$ ,  $^{107}\text{Sn}$ , and  $^{124}\text{La}$ , respectively. They are obtained by fitting the calculated momentum distributions in one dimension as, e.g.,  $p_x$  over the interval  $-100 \leq p_x \leq +100$  MeV/c with Gaussian functions. Choosing larger intervals leads to slightly higher temperatures, indicating that the distributions are not purely thermal and that several mechanisms may contribute. For  $-150 \leq p_x \leq +150$  MeV/c, the temperatures are higher by  $\approx 0.3$  MeV and for  $\pm 200$  MeV/c higher by  $\approx 0.5$  MeV than those obtained with the  $\pm 100$  MeV/c interval.

The weak dependence on the projectile is similar as in the experiment. The average value  $T = 4.5$  MeV is between 0.5 and 0.7 MeV higher than the experimental temperatures displayed in Fig. 16 and smaller than the microcanonical breakup temperature by about 1.5 MeV. It represents an average temperature as expected for an evaporation cascade produced by excited projectile fragments with initial temperatures close to the microcanonical temperatures. Extending the Gaussian fits over larger momentum intervals seems to increase the weight of sources with higher temperatures, including the small group of neutrons produced in the primary breakup (Fig. 19).

## V. DISCUSSION

### A. Bevalac data

Among the Bevalac data reported by the group of Madey *et al.*, results of measurements performed at small angles for the reactions Ne on Pb at 390 and 790 MeV/nucleon [18] and for Nb on Nb and Au on Au at 800 MeV/nucleon [20] are well suited for a comparison with the present data. Plastic detectors of 10 cm thickness with a width of 25 cm and a length of about 1 m were used, so that the  $0^\circ$  detectors positioned at 14.3 m from the target in the experiments with Nb and Au beams covered angles up to  $2.0^\circ$  with respect to the beam direction. In the experiments with Ne beams, the flight path was 8.0 m and the 1-m-long detector at  $0^\circ$  thus extended up to  $3.6^\circ$ . In the neutron spectra measured at these forward angles, a “striking peak” was discovered and found to be essentially independent of the projectile energy. The measured widths in the projectile frame were translated into source temperatures between 3.2 and 3.6 MeV and found to increase with decreasing impact parameter in the reactions with heavy projectiles [20].

These findings are in very good agreement with the results obtained in the present study (Figs. 13–15), indicating a universal property of the spectator decay at relativistic energies. Rapidity spectra in the moving frame for the four reactions studied at the Bevalac are compared with the  $^{124}\text{Sn} + \text{Sn}$  case in Fig. 20. With a normalization at the peak heights, the agreement is indeed impressive. The fall-off of the observed intensities toward larger rapidities is essentially identical for all five cases. On the low-energy side, at rapidities  $y - y_0 \leq -0.2$ , the different intensities of the Bevalac data presumably reflect different experimental conditions of the four experiments. In the present case of  $^{124}\text{Sn}$ , the peak is less symmetric and the slope toward smaller rapidity less steep.

Slopes extending toward midrapidity are expected for light particles at small angles in projectile fragmentations. This was, for example, shown for  $Z = 2$  particles from  $^{197}\text{Au}$  reactions at 1000 MeV/nucleon [32]. The slopes that are observed should depend strongly on the angular coverage [45]. The ALADIN spectrometer used

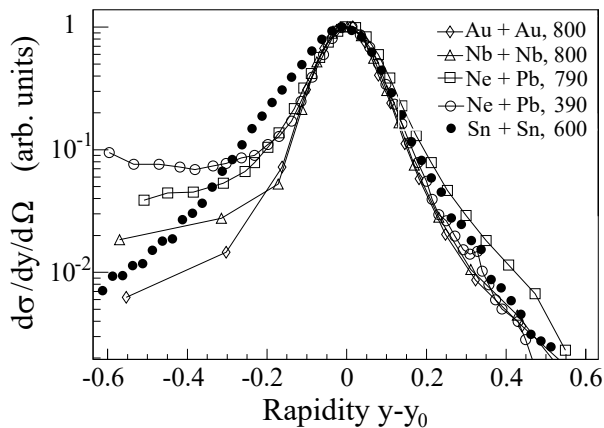


FIG. 20: Rapidity distributions in the projectile frame ( $y_0$  is the projectile rapidity) of neutrons at  $\theta_{\text{lab}} \leq 2^\circ$  from the present  $^{124}\text{Sn} + \text{Sn}$  fragmentation reaction (filled circles) in comparison with several reactions studied at the Bevalac [18, 20]. The distributions are normalized with respect to their maxima. The numbers in the legend indicate the projectile energies in MeV/nucleon.

in these experiments has an acceptance of  $\pm 10.2^\circ$  in the horizontal and  $\pm 4.5^\circ$  in the vertical direction (Sec. II A). In the Berkeley experiments, the acceptance was much more centered at  $0^\circ$ , thus apparently enhancing the detection of beam velocity neutrons with symmetric rapidity distributions. The slightly higher tail towards mid-rapidity observed with the coverage up to  $3.6^\circ$  in the experiments with Ne beams would support this interpretation (Fig. 20).

An alternative explanation for the modified slope appeared when the present data were compared with neutron time-of-flight spectra from the S107 test experiment which exhibit similar tails (Fig. 21). In this experiment, performed for investigating properties of LAND [40, 42, 43], beam-velocity neutrons were generated by Coulomb and diffractive dissociation of deuterons in Pb targets. The distance to LAND amounted to about 9.1 m which leads to slightly shorter flight times than in the present experiment but still permits a comparison of the peak structures. The tail to longer flight times recorded in S107 is not compatible with approximate symmetry in rapidity and thus not expected to originate from the breakup process.

The adopted explanation assumes that neutrons whose primary hits remain undetected produce delayed secondary hits after traveling through the detector for a certain time and possibly with reduced velocity. These hits if interpreted as the first hit of a neutron event in the detector will cause a shift to lower velocity for this event. Because half of the detector volume consists of iron the probability for neutron interactions not producing sufficient light for being recorded is not negligible. It is thus not excluded that the present spectra at rapidities below the peak rapidity are affected by the described experimental effect and thus not necessarily in contradiction

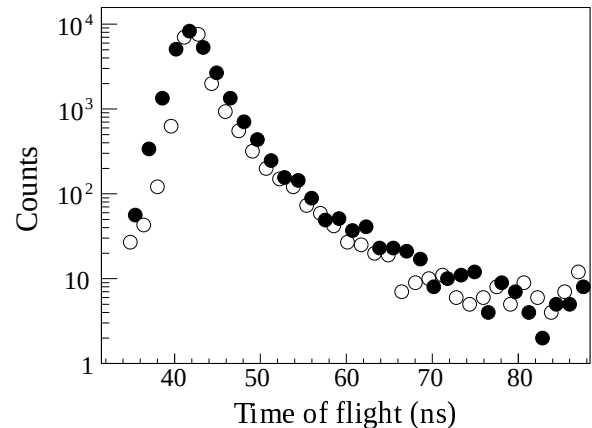


FIG. 21: Neutron time-of-flight spectra obtained in the present experiment (filled circles) and in experiment S107 with deuteron beams of 600 MeV/nucleon on a Pb target (open circles). The S107 distribution has been aligned in time and normalized at the peak.

to the universality visible also here in the Berkeley data (Fig. 20).

## B. Yields and temperatures

The measured rapidity distributions have wider-than-Gaussian tails (Fig. 20). Interpreting these shapes, Madey *et al.* have included additional Gaussians of larger widths to improve their description [18, 20]. Several choices were found equally successful, leaving this procedure somewhat arbitrary. One of the choices, however, included a Gaussian of width  $\sigma \approx 110$  MeV/ $c$  with an integrated strength comparable to that of the narrower peak. From the larger widths a momentum close to the Fermi momentum was obtained from the formula  $P = \sqrt{5}\sigma$  of the Goldhaber model [56].

It is assumed in this model that the product momenta in fast fragmentation processes may reflect the nucleonic Fermi motion within the colliding nuclei. The resulting momentum distributions are indistinguishable from that of a thermalized system with high temperatures of the order of 9 MeV. Indications for such processes were found experimentally, although with momentum distributions corresponding to significantly higher temperatures. Proton spectra measured for  $^{197}\text{Au} + ^{197}\text{Au}$  collisions at 1000 MeV/nucleon exhibit two components with an evaporation bump superimposed on flatter tails with extracted temperatures  $T \approx 6$  and  $\approx 25$  MeV for the two components, respectively [9]. Also the transverse momenta of light fragments in spectator decays measured in ALADIN experiments were found compatible with the Goldhaber model, the extracted temperatures  $T \approx 15$  MeV being somewhat closer to the expected value [32].

Comparable transverse-momentum widths for the fragmentation of  $^{197}\text{Au}$  and  $^{208}\text{Pb}$  projectiles at similar as

well as much higher incident energies were reported by Chance *et al.* [51] and Hüntrup *et al.* [52]. The deduced momentum widths exceed the expectation according to the Goldhaber model by factors up to about 2. Possible explanations for these excess widths were presented by Bauer [57]. Neutron components with comparable widths are difficult to identify in the present experiment because of the limited acceptance in transverse momentum. However, the measured rapidity distributions do not exclude their existence (Fig. 13).

The SMM does not contain equivalent mechanisms as part of the fragmentation process. In the model, a common temperature for all degrees of freedom of a given configuration is assumed. The present results for neutron emissions at forward angles thus indicates that, at medium and large  $Z_{\text{bound}}$ , the partitioning of the spectator sources into particles and fragments and their subsequent decay is sufficient to satisfactorily describe the multiplicities and temperatures observed for the low-temperature neutron component.

The observed difference of measured and calculated neutron multiplicities at smaller  $Z_{\text{bound}}$  was discussed in the previous section. It seems to indicate that the decay of the ensemble of excited sources with properties adjusted to reproduce the fragmentation data does not fully represent the production of spectator neutrons in these more violent collisions.

In a dynamical study based on the IQMD transport model, neutron multiplicities in qualitative agreement with the data measured for  $^{124}\text{Sn}$  and  $^{124}\text{La}$  fragmentations were obtained [58]. However, the location of the calculated neutron distributions at rapidities around 90% of the projectile rapidity, corresponding to  $p_z = 1057 \text{ MeV}/c$  or  $E_{\text{lab}} = 478 \text{ MeV}$ , is not consistent with the experimental observations (Figs 12 and 13). Presumably, secondary emissions from excited projectile fragments were not explicitly considered.

Combining the measured and calculated information and ignoring for this purpose the experimental uncertainty, an approximate neutron balance may be attempted. For mid-peripheral collisions with  $Z_{\text{bound}}$  in the interval 20 to 30, the neutron multiplicity measured for the spectator source is  $M_n = 11$  in the case of  $^{124}\text{Sn}$  fragmentations (Fig. 15). Following Pietrzak *et al.* [23], the size of the spectator system corresponding to  $Z_{\text{bound}} = 25$  is  $Z_{\text{spect}} \approx 30$ . In the participant-spectator picture, this leaves 20 charges from each of the two nuclei for the participant source. Applying again the relative abundance of nucleons and light charged particles measured by FOPI (cf. Sec. III A), one obtains a composition with 14 free protons, 26 protons and 29 neutrons bound in light charged particles, and 30 free neutrons in this source. Adding the 11 neutrons emitted by the projectile spectator (Fig. 15) and assuming  $\approx 10$  neutrons bound in multifragmentation products not accounted for in the model of Bertini [49] yields 51 neutrons, a value close to the prediction shown in Fig. 11. The neutrons emitted by the target spectator are assumed to be below the threshold

chosen in the calculations. It allows the conclusion that the flat neutron yields underneath the observed peaks, possibly with momenta reflecting the internal Fermi motion according to Goldhaber [56], are part of the participant source formed in the early stage of the reaction. The fact that this stage is not included in the SMM scenario, may also partly explain the underprediction of the neutron multiplicities at small  $Z_{\text{bound}}$  (Fig. 18).

## VI. SUMMARY

The production of neutrons at forward angles from the fragmentation and subsequent decay of the projectile spectators in reactions of  $^{124}\text{Sn}$ ,  $^{107}\text{Sn}$ , and  $^{124}\text{La}$  projectiles with Sn targets at 600 MeV/nucleon was investigated with the LAND detector positioned approximately 10 m downstream from the target of the ALADIN spectrometer. The identification and localization of neutrons with this detector followed the method presented in Ref. [40]. As reported there and discussed in the experimental sections, the multiplicity of neutrons in the present case of multi-neutron events cannot be determined better than with uncertainties of up to 20%. Because of the loss of neutrons between the target and the LAND detector of the order of 10%, the reported absolute neutron cross sections and multiplicities are possibly too low by an amount of that order.

A thermal source of neutrons traveling with nearly exactly beam velocity was identified. The temperatures between 2 and 5 MeV extracted from transverse momentum distributions measured with LAND do not indicate any visible dependence on the isotopic composition of the projectile. Their average value is in good agreement with the results obtained at the Bevalac and supports the invariance with projectile mass and energy observed there for incident energies between 390 and 800 MeV/nucleon [18, 20]. The observed invariance is expected within the more general concept of limiting fragmentation [59], presently being discussed up to the highest energies available for heavy-ion reactions (for recent references see, e.g., Ref. [60]). Regarding the yields of projectile fragments, it manifests itself in the universality observed for  $^{197}\text{Au}$  and  $^{208}\text{Pb}$  fragmentation at energies from several hundred MeV/nucleon up to 158 GeV/nucleon [32, 61, 62].

The neutron multiplicities measured at small  $Z_{\text{bound}}$ , i.e., small impact parameters, reflect the neutron-to-proton ratio  $N/Z$  of the projectile. They are, on average, 30% higher for the case of  $^{124}\text{Sn}$  than for the two neutron-poor projectiles, corresponding to the differences of their  $N/Z$  ratios. At large  $Z_{\text{bound}}$ , i.e., for reactions at large impact parameter leading to predominantly excited residues, the neutron multiplicities grow faster than in proportion to the absolute neutron numbers of the three projectiles. The different multiplicities represent the only isotopic effect of the neutron production observed in the present experiment.

The suitability of the ALADIN-LAND setup for the present purpose was studied with the Geant4 program package, using a simplified but in crucial dimensions accurate model geometry. Calculations were performed for neutron and fragment beams starting from the location of the target and with various properties, including moving thermal sources with temperatures up to 6 MeV. The calculations confirm that neutrons starting toward the high-efficiency volume defined within the detector volume of LAND arrive there with high probability without suffering interactions on their flight paths. The level of background from scattered neutrons with original directions other than toward the high-efficiency volume is small, of the order of 5% according to the estimates discussed in Sec. II D. With this limitation, the setup was found to be appropriate for the intended measurements, in retrospect justifying its use in earlier experiments [8, 9].

The statistical multifragmentation model (SMM) was used to calculate the neutron emission expected from ensemble calculations with parameters that permitted the successful interpretation of the fragment yields and correlations reported in Refs. [2, 23]. The predicted multiplicities for larger impact parameters are close to the observed values and correctly reflect the measured dependence on the isotopic composition of the projectile. The dependence on the choice made for the coefficient  $\gamma$  of the symmetry term of the liquid-drop description of the produced fragments was found to be small and significant only for the fragmentation of  $^{124}\text{Sn}$  projectiles. In this case, the multiplicity of evaporated neutrons is slightly decreasing for smaller values of  $\gamma$ , consistent with the simultaneous increase of the production of neutron-rich fragments [2]. The calculated temperatures with an average value  $T = 4.5$  MeV are between 0.5 and 0.7 MeV higher than the experimental values. The nearly negligible dependence on the neutron content of the projectile is similar as observed in the experiment.

The SMM description established in the fragmentation study performed for this experiment thus permits also very satisfactory predictions for neutrons, their multiplicities and source temperatures, at least for medium and large impact parameters. The underprediction of the observed neutron multiplicities at smaller impact parameters seems to indicate that the decay of the ensemble of excited sources can only partly account for the production of spectator neutrons at forward angles in these more violent collisions.

### Acknowledgments

A.S.B. is grateful to FIAS Frankfurt, the GSI Helmholtzzentrum Darmstadt, and the IKP of Mainz University for support and hospitality. R.O. thanks TUBITAK-DFG cooperation for financial support. C.Sf. acknowledges support by an Alexander-von-Humboldt fellowship. This work was supported by the European Community under Contract No. HPRI-CT-1999-00001,

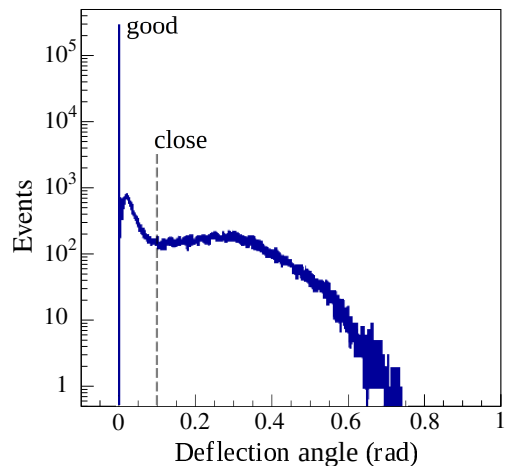


FIG. 22: Distribution of displacements of 600-MeV neutrons from a source located at the target position and emitting isotropically within the solid angle given by  $\theta_{\text{lab}} \leq 15^\circ$ , expressed as apparent changes of the angle of emission as viewed from the target. Deflection angles different from zero are caused by scattering processes experienced by the neutrons along their trajectories to the test plane. The labels “good” and “close”, respectively, indicate that no scattering occurred and that, in the case of a scattering process, the final apparent direction is within a cone of  $\leq 0.1$  rad ( $5.7^\circ$ ) with respect to the initial direction (dashed line).

by the French-German Collaboration Agreement between IN2P3 - DSM/CEA and GSI, by the Polish Ministry of Science and Higher Education under Contracts No. N202 160 32/4308 (2007-2009) and No. 1 P03B 020 30 (2006-2009), and by the Swedish Research Council under Contract No. 2022-04248.

### VII. APPENDIX: STUDY OF THE DETECTION EFFICIENCY WITH GEANT4

An extended study of the experimental ALADIN-LAND setup with calculations within the Geant4 framework [41] was performed to document its suitability for measuring neutron emissions in spectator decay. The elements of the spectrometer contain significant amounts of iron and other materials that are not directly shadowing LAND from the target position but are potential sources of background of neutrons and other particles produced by scattering and inelastic processes of neutrons emitted from the target. The ALADIN magnet, at the same time, serves as an effective shield by absorbing neutrons from the mid-rapidity source, emitted at larger polar angles in more central collisions.

The model of the experimental setup generated for this purpose was based on the measured dimensions and positions of the major components available with precisions on the level of  $\pm 1$  mm. Minor components were represented with their geometries simplified, inhomogeneous surfaces smoothed, and technical details omitted, all un-

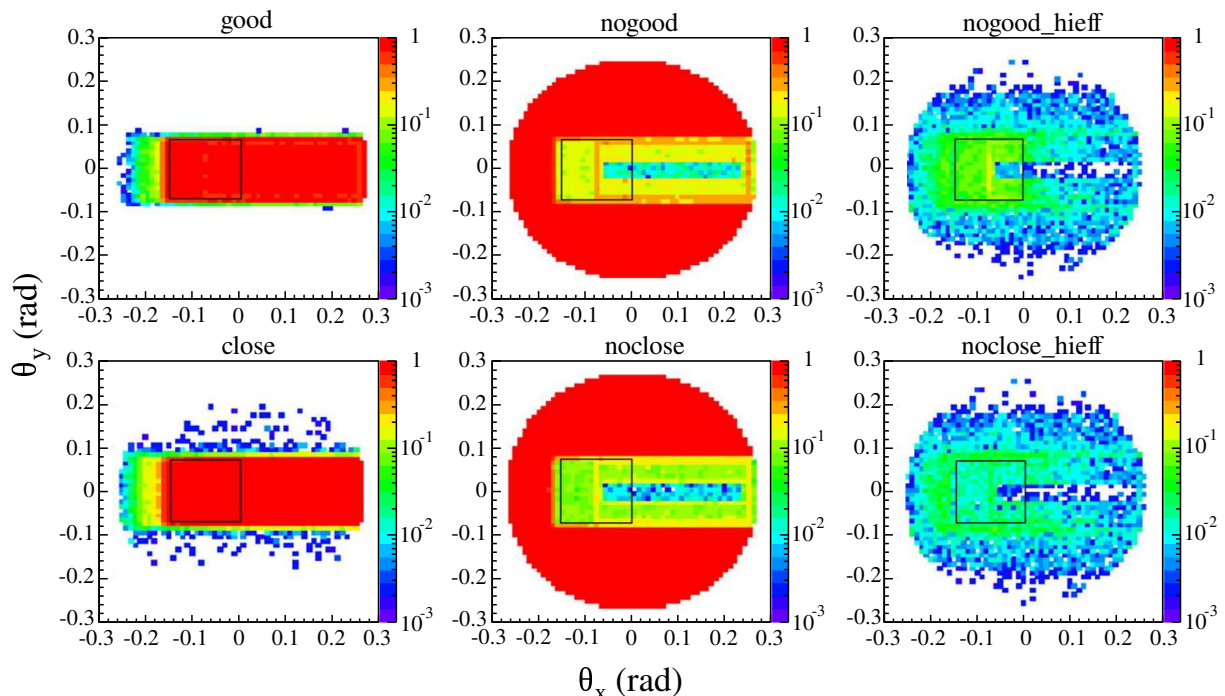


FIG. 23: Original directions with respect to the beam direction of 600-MeV neutrons from a source located at the target position and emitting isotropically within the solid angle given by  $\theta_{\text{lab}} \leq 15^\circ$ , sorted according to the scatterings experienced along their trajectories to the test plane (see text for explanations). The black square represents the high-efficiency area plotted in the chosen coordinate system in which the negative  $x$  direction viewed from the target position points to the right.

der the condition that the total amount of material is preserved. The model was divided into the substructures ALADIN magnet, the vacuum and detector chambers, and the time-of-flight wall. The floor of and the air in the experimental vault was included as well. For evaluating the resulting effects, a test plane perpendicular to the primary beam direction at the location of the front plane of LAND was added to the model. Within this plane, a high-efficiency area was defined with the lateral dimensions of the high-efficiency volume (Sec. II C).

The first set of calculations was aimed at determining the scattering probabilities as a function of the emission angle from the target position. Pencil beams of neutrons with energies between 400 and 800 MeV were used for homogeneously scanning a cone of polar angles  $\theta_{\text{lab}} \leq 15^\circ$ . Their trajectories and those of produced secondary particles were followed and, if they were not absorbed earlier, registered with their positions on the test plane. Examples of the results obtained for 600-MeV neutrons are given in the following. They are different from those given in Sec. II D because the homogeneous solid-angle coverage chosen here is different from that produced by moving thermal sources (see below).

More than half of the neutrons emitted into the  $15^\circ$  cone are absorbed by the magnet and other parts of the setup and only about 37% arrive at the test plane according to the calculations. The displacements at the test plane caused by scattering processes are presented as angles of deflection with respect to the original direc-

tion of emission as viewed from the target position. The resulting distribution for  $10^6$  neutrons emitted within the defined cone is shown in Fig. 22. The label “good” in the figure indicates that no scattering has occurred. It is the case for approximately 70% of the number of neutrons reaching the test plane. Small deflections form a narrow bump contained within 0.05 rad, followed by a wider distribution with a broad maximum close to 0.3 rad. The label “close” includes processes causing deflections up to 0.1 rad ( $5.7^\circ$ ), primarily produced by interactions within the time-of-flight wall and the exit flange of the detector chamber (cf. Fig. 4).

The observed effects are presented in Fig. 23 in the form of probabilities for the absence of any scattering (“good”), the occurrence of small-angle scatterings (“close”) and for their complements (“nogood” and “noclose”). In addition, the latter two groups are also tested for whether the neutron finally passes through the high-efficiency area and, with this condition met, plotted in the right column. The color code representing the probabilities within the two-dimensional plane of original emission angles is logarithmic and the same for all six cases.

The main observation is apparent in the left column of Fig. 23. Neutrons can reach the test plane without scattering or with small deflections essentially only if they start toward the window defined by the poles, yoke and vacuum chamber of the ALADIN magnet. The high-efficiency area is contained within this window. However about 20% of the neutrons emitted toward the high-

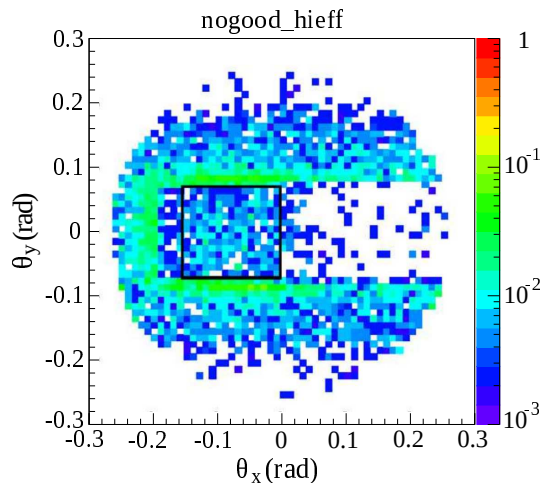


FIG. 24: Probability distribution of the original directions with respect to the beam direction of 600-MeV neutrons from a source, located at the target position and emitting isotropically within the solid angle given by  $\theta_{\text{lab}} \leq 15^\circ$ , in a virtual setup including only the ALADIN magnet and the air within the vault. Events are recorded under the condition that a scattering occurs and the scattered neutron enters the high-efficiency area of the test plane represented by the black square.

efficiency window will suffer a scattering process (top-middle panel “nogood”). About one half of them (probability 10%) will still hit the high-efficiency area (top-right panel), most likely with only a minor deflection because the probability for being emitted toward the high-efficiency area and still hitting it after a deflection by more than 0.1 rad (“noclose”) is on the level of 2% or less (bottom-right panel of Fig. 23). The narrow horizontal band with reduced scattering probability visible in the middle and right columns shows the effect of the thin window of 1-mm steel welded into the rear wall of the detector chamber (Fig. 1). Viewed from the target position, its vertical width of 28 cm corresponds to angles of  $\pm 22$  mrad.

The modular structure of the setup as reproduced for the calculations made it possible to study the effects of individual components. As an example, results obtained by activating only the ALADIN magnet together with the floor of and the air within the vault are shown in Fig. 24. It gives again the probabilities for scattered neutrons reaching the high-efficiency area as a function of their original directions but under the condition that only the magnet is present. The magnet cannot affect neutrons emitted towards the high-efficiency area. Scattering processes in the air of the vault are responsible for the intensity of 1% or less visible within the black square representing the high-efficiency area. Neutrons emitted into other directions are scattered into the high-efficiency area with very similar probability. Bands of higher intensity ( $\approx 5\%$ ) are produced by neutrons emitted towards

the upper and lower edges of the magnet poles and magnet chamber and scattered into the high-efficiency area. The figure may be compared with the corresponding figure with the full setup shown in the top-right panel of Fig. 23.

More realistic emission profiles were modeled with thermal sources of temperatures up to 6 MeV moving with the projectile velocity. Examples of results for the 4-MeV source were already included in the main text (Sec. II D). The initial distribution of emissions (Fig. 3), the spectrum of deflections (Fig. 4), and the distribution of scattered neutrons entering the high-efficiency area (Fig. 5) are shown there. The essential results are very similar to those shown in Fig. 23. The scattering probabilities as a function of the initial directions are necessarily the same but the fewer emissions at larger polar angles reduce the overall background intensity, thus leading to the smaller values given in Sec. II D and the narrower distribution of deflections shown in Fig. 4.

A final set of calculations was performed with fragment beams emitted from the target and bent by the magnet into directions close to that of the deflected primary projectiles. The aim was to follow the history of fragments produced in the target and traveling toward the time-of-flight wall and exit flange of the detector chamber. Interactions with the light nuclei of the plastic time-of-flight detectors can be expected to produce mainly excited fragment residues, evaporating neutrons into narrow cones in their flight directions. Fragments with transverse momenta in vertical directions large enough for them to miss the thin exit window installed for the projectile beam may undergo more violent reactions with the thicker steel parts of the chamber.

For investigating the level of background to be expected from these processes, the Bertini model [49] was selected from the physics list of Geant4 (cf. Fig. 11). The majority of secondary neutrons originates from evaporation into a narrow cone of directions with respect to the direction of the emitting fragment and most likely from a position somewhere in the time-of-flight wall or exit flange of the detector chamber. It was found that the probability for reaching the high-efficiency volume of LAND is at most a few percent per fragment or  $\alpha$  particle, and concentrated on the side of the deflected beam. With the measured  $\alpha$  and IMF multiplicities, this will add up to not more than typically 10 %, i.e.  $\approx 0.1$  neutron per event. Extrapolation from the high-efficiency volume to the full phase space of the projectile source increases this value by a factor of roughly 3. It still permits the conclusion that secondary reactions of projectile fragments in the time-of-flight wall or the exit flange are not significantly enlarging the background. The latter consists mainly of neutrons produced in the target and undergoing scattering processes somewhere along their trajectories.

- 
- [1] C. Sfienti, P. Adrich, T. Aumann, C. O. Bacri, T. Barczyk, R. Bassini *et al.*, Phys. Rev. Lett. **102**, 152701 (2009).
- [2] R. Ogul, A. S. Botvina, U. Atav, N. Buyukcizmeci, I. N. Mishustin, P. Adrich *et al.*, Phys. Rev. C **83**, 024608 (2011); **85**, 019903(E) (2012), Erratum.
- [3] J. P. Bondorf, A. S. Botvina, A. S. Iljinov, I. N. Mishustin, and K. Sneppen, Phys. Rep. **257**, 133 (1995).
- [4] A. Le Fèvre, G. Auger, M. L. Begemann-Blaich, N. Bellaïze, R. Bittiger, F. Bocage *et al.*, Phys. Rev. Lett. **94**, 162701 (2005).
- [5] D. Henzlova, A. S. Botvina, K.-H. Schmidt, V. Henzl, P. Napolitani, and M. V. Ricciardi, J. Phys. G **37**, 085010 (2010).
- [6] Th. Blaich, Th. W. Elze, H. Emling, H. Freiesleben, K. Grimm, W. Henning *et al.*, Nucl. Instrum. Methods Phys. Res. Sect. A **314**, 136 (1992).
- [7] A. S. Botvina, I. N. Mishustin, M. Begemann-Blaich, J. Hubele, G. Imme, I. Iori *et al.*, Nucl. Phys. A **584**, 737 (1995).
- [8] J. Pochodzalla, T. Möhlenkamp, T. Rubehn, A. Schüttauf, A. Wörner, E. Zude *et al.*, Phys. Rev. Lett. **75**, 1040 (1995).
- [9] T. Odeh, R. Bassini, M. Begemann-Blaich, S. Fritz, S. J. Gaff-Ejakov, D. Gourio *et al.*, Phys. Rev. Lett. **84**, 4557 (2000).
- [10] V. E. Viola and R. Bougault, Eur. Phys. J. A **30**, 215 (2006).
- [11] U. Jahnke, G. Ingold, H. Homeyer, M. Bürgel, Ch. Egelhaaf, H. Fuchs, and D. Hilscher, Phys. Rev. Lett. **50**, 1246 (1983).
- [12] J. Galin and U. Jahnke, J. Phys. G **20**, 1105 (1994).
- [13] G. J. Kunde, S. J. Gaff, C. K. Gelbke, T. Glasmacher, M. J. Huang, R. Lemmon *et al.*, Phys. Rev. Lett. **77**, 2897 (1996).
- [14] L. G. Sobotka, R. J. Charity, D. K. Agnihotri, W. Gawlikowicz, T. X. Liu, W. Lynch, U. Schröder, J. Töke, and H. S. Xu, Phys. Rev. C **62**, 031603(R) (2000).
- [15] S. Wuenschel, K. Hagel, R. Wada, J. B. Natowitz, S. J. Yennello, Z. Kohley *et al.*, Nucl. Instrum. Methods Phys. Res. Sect. A **604**, 578 (2009).
- [16] P. Morfouace, C. Y. Tsang, Y. Zhang, W. G. Lynch, M. B. Tsang, D. D. S. Coupland *et al.*, Phys. Lett. B **799**, 135045 (2019).
- [17] R. A. Cecil, B. D. Anderson, A. R. Baldwin, R. Madey, W. Schimmerling, J. W. Kast, and D. Ortendahl, Phys. Rev. C **24**, 2013 (1981).
- [18] R. Madey, J. Varga, A. R. Baldwin, B. D. Anderson, R. A. Cecil, G. Fai, P. C. Tandy, J. W. Watson, and G. D. Westfall, Phys. Rev. Lett. **55**, 1453 (1985).
- [19] A. R. Baldwin, R. Madey, W.-M. Zhang, B. D. Anderson, D. Keane, J. Varga, J. W. Watson, G. D. Westfall, K. Frankel, and C. Gale Phys. Rev. C **46**, 258 (1992).
- [20] R. Madey, W.-M. Zhang, B. D. Anderson, A. R. Baldwin, B. S. Flanders, W. Pairsuwan, J. Varga, J. W. Watson, and G. D. Westfall, Phys. Rev. C **38**, 184 (1988).
- [21] M. M. Htun, R. Madey, W. M. Zhang, M. Elaasar, D. Keane, B. D. Anderson, A. R. Baldwin *et al.*, Phys. Rev. C **59**, 336 (1999).
- [22] Jun Su, W. Trautmann, Long Zhu, Wen-Jie Xie, and Feng-Shou Zhang, Phys. Rev. C **98**, 014610 (2018).
- [23] T. Pietrzak, A. S. Botvina, J. Brzychczyk, N. Buyukcizmeci, A. Le Fèvre, J. Lukasik, P. Pawłowski, C. Sfienti, W. Trautmann, and A. Wieloch, Phys. Lett. B **809**, 135763 (2020).
- [24] J. Brzychczyk, T. Pietrzak, A. Wieloch, and W. Trautmann, Phys. Rev. C **98**, 054606 (2018).
- [25] Jun Su, Long Zhu, and Erxi Xiao, Phys. Rev. C **105**, 024608 (2022).
- [26] Erxi Xiao, Yujie Feng, Xin Lei, Long Zhu, and Jun Su, J. Phys. G **49**, 065102 (2022).
- [27] D. Henzlova, K. H. Schmidt, M. V. Ricciardi, A. Kelić, V. Henzl, P. Napolitani *et al.*, Phys. Rev. C **78**, 044616 (2008).
- [28] V. Föhr, A. Bacquias, E. Casarejos, T. Enqvist, A. R. Junghans, A. Kelić-Heil *et al.*, Phys. Rev. C **84**, 054605 (2011).
- [29] H. Imal, A. Ergun, N. Buyukcizmeci, R. Ogul, A. S. Botvina, and W. Trautmann, Phys. Rev. C **91**, 034605 (2015).
- [30] H. Geissel, P. Armbruster, K. H. Behr, A. Brünle, K. Burkard, M. Chen *et al.*, Nucl. Instrum. Methods Phys. Res. Sect. B **70**, 286 (1992).
- [31] J. Lukasik, P. Adrich, T. Aumann, C. O. Bacri, T. Barczyk, R. Bassini *et al.*, Nucl. Instrum. Methods Phys. Res. Sect. A **587**, 413 (2008).
- [32] A. Schüttauf, W.D. Kunze, A. Wörner, M. Begemann-Blaich, Th. Blaich, D. R. Bowman *et al.*, Nucl. Phys. A **607**, 457 (1996).
- [33] G. J. Kunde, W. C. Hsi, W. D. Kunze, A. Schüttauf, A. Wörner, M. Begemann-Blaich *et al.*, Phys. Rev. Lett. **74**, 38 (1995).
- [34] C. Sfienti, P. Adrich, T. Aumann, C.O. Bacri, T. Barczyk, R. Bassini *et al.*, Nucl. Phys. A **749**, 83c (2005).
- [35] G. Bauer, F. Bieser, F. P. Brady, J. C. Chance, W. F. Christie, M. Gilkes *et al.*, Nucl. Instrum. Methods Phys. Res. Sect. A **386**, 249 (1997).
- [36] H. Sann, Nucl. Instrum. Methods Phys. Res. Sect. A **392**, 433 (1997).
- [37] C. Sfienti, J. Lühning, U. Lynen, W. F. J. Müller, A. Mykulyak, T. Barczyk *et al.*, in *Proceedings of the XLI International Winter Meeting on Nuclear Physics*, Bormio, Italy, edited by I. Iori and A. Moroni, Ricerca Scientifica ed Educazione Permanente Suppl. 120 (University of Milan, Milan, 2003), p. 323.
- [38] J. Hubele, P. Kreutz, J. C. Adloff, M. Begemann-Blaich, P. Bouissou, G. Imme *et al.*, Z. Phys. A **340**, 263 (1991).
- [39] C. A. Ogilvie, J. C. Adloff, M. Begemann-Blaich, P. Bouissou, J. Hubele, G. Imme *et al.*, Phys. Rev. Lett. **67**, 1214 (1991).
- [40] P. Pawłowski, J. Brzychczyk, Y. Leifels, W. Trautmann, P. Adrich, T. Aumann *et al.*, Nucl. Instrum. Methods Phys. Res. Sect. A **694**, 47 (2012).
- [41] S. Agostinelli, J. Allison, K. Amako, J. Apostolakis, H. Araujo, P. Arce *et al.*, Nucl. Instrum. Methods Phys. Res. Sect. A **506**, 250 (2003).
- [42] K. Boretzky, A. Grünschloß, S. Ilievski, P. Adrich, T. Aumann, C. A. Bertulani *et al.*, Phys. Rev. C **68**, 024317 (2003).
- [43] Th. Blaich, B. Dechant *et al.*, GSI Scientific Report 1992, page 375; <https://repository.gsi.de/record/53539/files/GSI->

- Report-1993-1.pdf.
- [44] K. Boretzky, I. Gašparić, M. Heil, J. Mayer, A. Heinz, C. Caesar *et al.*, Nucl. Instrum. Methods Phys. Res. Sect. A **1014**, 165701 (2021).
  - [45] O. Yordanov, K. Gunzert-Marx, P. Adrich, T. Aumann, K. Boretzky, H. Emling *et al.*, Nucl. Instrum. Methods Phys. Res. Sect. B **240**, 863 (2005).
  - [46] D. H. E. Gross, Rep. Prog. Phys. **53**, 608 (1990).
  - [47] P. Kreutz, J. C. Adloff, M. Begemann-Blaich, P. Bouissou, J. Hubele, G. Imme *et al.*, Nucl. Phys. A **556**, 672 (1993).
  - [48] J. A. Hauger, B. K. Srivastava, S. Albergo, F. Bieser, F. P. Brady, Z. Caccia *et al.*, Phys. Rev. C **62**, 024616 (2000).
  - [49] A. Heikkinen, N. Stepanov, and J. P. Wellisch, in *Proceedings of 2003 Conference for Computing in High Energy and Nuclear Physics* <https://cds.cern.ch/record/597895>, La Jolla, California, USA, preprint arXiv:nucl-th/0306008 (2003).
  - [50] W. Reisdorf, A. Andronic, R. Averbeck, M. L. Benabderrahmane, O. N. Hartmann, N. Herrmann *et al.*, Nucl. Phys. A **848**, 366 (2010).
  - [51] J. L. Chance, F. P. Brady, J. L. Romero, S. Albergo, F. Bieser, Z. Caccia *et al.*, Phys. Rev. C **64**, 014610 (2001).
  - [52] G. Hüntrup, T. Streibel, and W. Heinrich, Phys. Rev. C **65**, 014605 (2001).
  - [53] Hongfei Xi, T. Odeh, R. Bassini, M. Begemann-Blaich, A. S. Botvina, S. Fritz *et al.*, Z. Phys. A **359**, 397 (1997); H. Xi *et al.*, Eur. Phys. J. A **1**, 235 (1998), Erratum.
  - [54] W. Trautmann, R. Bassini, M. Begemann-Blaich, A. Ferrero, S. Fritz, S. J. Gaff-Ejakov *et al.*, Phys. Rev. C **76**, 064606 (2007).
  - [55] R. Nepeivoda, A. Svetlichnyi, N. Kozyrev, and I. Pshenichnov, Particles **5**, 40 (2022).
  - [56] A. S. Goldhaber, Phys. Lett. **53B**, 306 (1974).
  - [57] W. Bauer, Phys. Rev. C **51**, 803 (1995).
  - [58] S. Kumar and Y. G. Ma Phys. Rev. C **86**, 051601(R) (2012).
  - [59] J. Benecke, T. T. Chou, C. N. Yang, and E. Yen, Phys. Rev. **188**, 2159 (1969).
  - [60] B. Kellers and G. Wolschin, Eur. Phys. J. A **57**, 47 (2021).
  - [61] M. L. Cherry, A. Dabrowska, P. Deines-Jones, R. Holynski, W. V. Jones, E. D. Kolganova *et al.*, Phys. Rev. C **52**, 2652 (1995).
  - [62] G. Hüntrup, T. Streibel, and W. Heinrich, Phys. Rev. C **61**, 034903 (2000).